



THESIS  
2  
2000



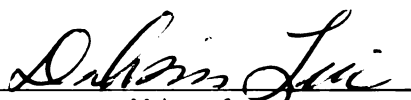
This is to certify that the  
dissertation entitled

Analysis of Composite Laminates  
By Moire Interferometry  
presented by

Elias Ruda Shakour

has been accepted towards fulfillment  
of the requirements for

Ph.D. degree in Engineering Mechanics



Major professor

Date May 5, 2000

**PLACE IN RETURN BOX** to remove this checkout from your record.  
**TO AVOID FINES** return on or before date due.  
**MAY BE RECALLED** with earlier due date if requested.

| DATE DUE | DATE DUE | DATE DUE |
|----------|----------|----------|
|          |          |          |
|          |          |          |
|          |          |          |
|          |          |          |
|          |          |          |
|          |          |          |
|          |          |          |
|          |          |          |
|          |          |          |
|          |          |          |
|          |          |          |
|          |          |          |
|          |          |          |
|          |          |          |
|          |          |          |
|          |          |          |
|          |          |          |
|          |          |          |
|          |          |          |
|          |          |          |
|          |          |          |

**ANALYSIS OF COMPOSITE LAMINATES BY MOIRE INTERFEROMETRY**

**By**

**Elias Ruda Shakour**

**A DISSERTATION**

**Submitted to  
Michigan State University  
in partial fulfillment of the requirements  
for the degree of**

**DOCTOR OF PHILOSOPHY**

**Materials Science and Mechanics**

**2000**



## **ABSTRACT**

### **ANALYSIS OF COMPOSITE LAMINATES BY MOIRE INTERFEROMETRY**

By

Elias Ruda Shakour

Composite laminates are organized by laminae with various fiber orientations. The sudden change of material properties across laminate interfaces is of an inherent characteristic of composite laminates. As a result of material property mismatch through the laminate thickness, high stresses and strains could take place on laminate interfaces. They are especially significant around free edges of composite laminates. In order to examine the stresses and strains with high gradients in composite laminates, an accurate measuring method is required. Due to its high sensitivity, moire interferometry has been useful for in-plane displacement measurements. Since moire interferometry is a surface method, its measurements are purely of surface conditions. The feasibility of the surface method for general structural analysis has become a serious question. This study was focused on validation and applications of moire interferometry. It was divided into three sections. In the first section, the existing two-layer grating technique was simplified to one-layer technique aiming at reducing the reinforcement effect of moire grating on testing specimens. A further study on no-layer grating was also explored for a possible combination of moire interferometry and photoelasticity. It was believed that the combined technique

could provide two independent measurements for mutual verification. The one-layer grating technique was then used in the second section of free-edge investigation. Composite beams with various widths were subjected to four-point bending. Experimental results revealed that the normal strains were independent of the beam width. However, the shear strains were significantly increased as the beam width decreased, signaling the free-edge effect. Comparisons based on composite beams made of different materials and laminations verified that free-edge effect was more significant in composite laminates with higher material property mismatch among laminae. In fact, the depth of boundary layer was proportional to the level of material properties mismatch. Based on the conclusion that the normal strains were insensitive to the free-edge effect, many assembled composite beams were investigated by moire interferometry in the third section. Various assembling techniques such as mechanical riveting, adhesive bonding, stitching joining and their combinations were used for joining two composite beams together. Experimental results combined with analytical modeling investigated, i.e. the interface model and the interphase model, presented an effective way to express the joining force of each assembled composite beam. It was concluded that mechanical riveting was an efficient assembling technique, at least for the composite laminates used in the study.

Copyright by  
Elias Ruda Shakour  
2000

**To my wife Sana and my daughter Yasmeeen, whose affection has been a continuous energy during of these courses of studies. To my parents Ruda and Miriam who taught me responsibility and courage.**

## **ACKNOWLEDGMENTS**

The author wishes to express his sincerest appreciation and gratitude to his academic and major advisor Professor Dahsin Liu for his valuable guidance, encouragement and advise in personal as well as professional matters during the course of this research. Professor Liu has unselfishly shared with the author his greatest attribute, creativity, and an invaluable tool that few possess. The author also extends his appreciation to the guidance committee members Dr. Tim Hogan, Dr. Patrick Kown, and Dr. Stanley Flegler.

Special appreciation and love is extended to the author's wife, Sana, for consistent encouragement, understanding, patience and love throughout his graduate career; the author's daughter, Yasmeen for spiritually strengthening the author; his parents for inspiration and support; his brothers and sisters Hania, Gabriel, Nasser, Amira, and Laila for the patience, love, and support.

# TABLE OF CONTENTS

|   |            |
|---|------------|
| <b>ACKNOWLEDGMENTS .....</b>                                    | <b>vi</b>  |
| <b>TABLE OF CONTENTS .....</b>                                  | <b>vii</b> |
| <b>LIST OF TABLES .....</b>                                     | <b>x</b>   |
| <b>LIST OF FIGURES .....</b>                                    | <b>xi</b>  |
| <b>Chapter 1 .....</b>  | <b>1</b>   |
| <b>MOIRE INTERFEROMETRY .....</b>                               | <b>1</b>   |
| Introduction.....   | 1          |
| Background .....  | 2          |
| Geometric moire .....   | 2          |
| Moire interferometry.....                                       | 4          |
| Literature review .....   | 8          |
| Diffraction grating.....  | 8          |
| Applications of moire interferometry.....                       | 10         |
| Objectives.....   | 12         |
| Organization .....  | 13         |
| References .....  | 14         |
| <b>Chapter 2 .....</b>  | <b>17</b>  |
| <b>COMBINING MOIRE INTERFEROMETRY AND PHOTOELASTICITY .....</b> | <b>17</b>  |
| Abstract .....  | 17         |
| Introduction.....   | 18         |
| Grating techniques .....  | 20         |
| Two-layer grating .....   | 20         |
| Conventional technique .....                                    | 20         |
| Modified technique .....  | 21         |
| One-layer grating .....   | 21         |
| Zero-layer grating.....   | 24         |
| Combining moire and photoelasticity.....                        | 26         |
| Transmission photoelasticity .....                              | 26         |
| Reflection photoelasticity .....                                | 30         |
| Single coating for both moire and photoelasticity.....          | 30         |
| Case studies.....   | 33         |
| Effects of coating thickness.....                               | 33         |
| Stress concentration .....                                      | 36         |
| Summary .....   | 41         |

|   |            |
|---|------------|
| Acknowledgements .....  | 41         |
| References .....  | 43         |
| <b>Chapter 3 .....</b>  | <b>46</b>  |
| <b>MISMATCH OF MATERIAL PROPERTIES AND FREE-EDGE EFFECT .....</b> | <b>46</b>  |
| Abstract .....  | 46         |
| Free-edge effect .....  | 47         |
| Moire interferometry .....  | 49         |
| Experimental investigations .....                                 | 52         |
| Moire on composite laminates .....                                | 52         |
| Materials and testing .....                                       | 53         |
| Effects of specimen width .....                                   | 54         |
| Mismatch of material properties .....                             | 55         |
| Results and discussions .....                                     | 56         |
| Strain Calculations .....   | 56         |
| $\gamma_{xy}$ based on strain-displacement relations .....        | 58         |
| $\gamma_{xy}$ Based on vector analysis .....                      | 60         |
| Depth of Boundary Layer .....                                     | 63         |
| Effect of material type .....                                     | 67         |
| Effect lamination type .....                                      | 72         |
| Conclusions .....   | 73         |
| Acknowledgements .....  | 74         |
| References .....  | 75         |
| <b>Chapter 4 .....</b>  | <b>77</b>  |
| <b>JOINING FORCES IN ASSEMBLED COMPOSITE BEAMS .....</b>          | <b>77</b>  |
| Abstract .....  | 77         |
| Introduction .....  | 78         |
| Analytical modeling .....   | 79         |
| The interface model .....   | 79         |
| The interphase model .....  | 84         |
| Experimental investigations .....                                 | 87         |
| Composite laminates .....   | 87         |
| Joining techniques .....  | 88         |
| Moire interferometry .....  | 92         |
| Results and conclusions .....                                     | 96         |
| Moire fringe patterns .....                                       | 96         |
| Maximum joining force .....                                       | 102        |
| Singular points .....   | 109        |
| Joining forces .....  | 112        |
| Conclusions .....   | 114        |
| Acknowledgments .....   | 115        |
| References .....  | 117        |
| <b>Chapter 5 .....</b>  | <b>118</b> |

|  |            |
|--|------------|
| <b>CONCLUSIONS AND RECOMENDATIONS.....</b>               | <b>118</b> |
| Major conclusions.....                                   | 119        |
| Chapter two.....   | 119        |
| Chapter three.....                                       | 120        |
| Chapter four.....  | 121        |
| Recommendations for future work.....                     | 121        |
| <b>APPENDIX A.....</b>                                   | <b>124</b> |
| <b>Procedures for aluminum evaporation .....</b>         | <b>124</b> |
| <b>APPENDIX B .....</b>                                  | <b>126</b> |
| <b>Moire fringe patterns used for subtractions .....</b> | <b>126</b> |
| Combining moire interferometry and photoelasticity.....  | 126        |
| Joining forces in assembled composites .....             | 127        |
| Mismatch of materials and the free edge effect.....      | 130        |



# LIST OF TABLES

## Chapter 4

Table 4. 1- Comparisons of joining forces ..... 113

## LIST OF FIGURES

### Chapter 1

|   |   |
|---|---|
| Figure 1.1- Moire fringe patterns from various shapes of patterns overlapping one another ..... | 3 |
| Figure 1.2- Schematic diagram for geometrical moire formation.....                              | 5 |
| Figure 1.3 - Schematic diagram of moire interferometry .....                                    | 7 |

### Chapter 2

|  |    |
|--|----|
| Figure 2.1- Schematic diagram of optical setup for moire interferometry (horizontal two beams only). .....   | 19 |
| Figure 2.2- Schematic diagrams of specimen with (a) two-layer grating, (b) one-layer grating, and (c) zero-layer grating .....   | 22 |
| Figure 2. 3 - U-displacement moire fringe patterns from four-point bend tests for (a) polished aluminum specimen and (b) transparent PSM-5A specimen.....  | 25 |
| Figure 2. 4 - Schematic diagram of processing setup for casting a specimen with zero-layer grating.....  | 27 |
| Figure 2.5 - Schematic diagram of optical setup for combining moire interferometry and transmission photoelasticity. ....  | 28 |
| Figure 2.6 - Fringe patterns of PSM-5A beam under four-point bending: (a) transmission isochromatic fringes, (b) U-displacement fringes, and (c) simultaneous recording of photoelasticity and moire fringes .....                   | 29 |
| Figure 2.7 - Schematic diagram of optical setup for combining moire interferometry and reflection photoelasticity.....   | 31 |
| Figure 2.8 - Fringe patterns of a PSM-5A beam under four point bending: (a) reflection isochromatic fringes, (b) U-displacement fringes, and (c) simultaneous recording of photoelasticity and moire fringes. ....                   | 32 |
| Figure 2.9 - Fringe patterns of a glass/epoxy beam with PL8 moire photoelasticity coating (a) reflection isochromatic fringes, (b) U-displacement fringes, and (c) simultaneous recording of photoelasticity and moire fringes. .... | 34 |
| Figure 2.10 - Moire fringe patterns of glass/epoxy beams with PL8 grating thickness of (a) 0.55 mm, (b) 1.36 mm, and (c) 3.17 mm.....  | 35 |

|  |    |
|--|----|
| Figure 2.11 - Photoelasticity fringe patterns of glass/epoxy beams with PL8 grating thickness of (a) 0.55 mm (b) 1.36 mm, and (c) 3.17 mm.....   | 37 |
| Figure 2.12 - Fringe patterns of a notched glass/epoxy beam with PL8 moire-photoelasticity coating (a) reflection isochromatic fringes, (b) U - displacement fringes, and (c) simultaneous recording of photoelasticity and moire fringes..... | 38 |
| Figure 2.13 - Schematic diagram of finite element model for the beam with central hole; it has 1482 elements, the element type is 8 node element of CPS8R, .....   | 39 |
| Figure 2.14 - Comparisons of results from moire interferometry, photoelasticity, and finite element analysis. ....   | 40 |

### Chapter 3

|  |    |
|--|----|
| Figure 3.1 - Schematic diagram of optical setup for moire interferometry (horizontal two beams only). .... | 51 |
| Figure 3.2 - Moire fringe patterns for graphite/epoxy laminates with three different widths .....          | 57 |
| Figure 3.3 - Calculation of shear strain on the laminate interface based on least square method.....       | 59 |
| Figure 3.4 - Shear strain calculations based on vector analysis.....                                       | 61 |
| Figure 3.5 - Distribution of $\epsilon_{xx}$ through laminate thickness .....                              | 64 |
| Figure 3.6 - Distribution of $\epsilon_{yy}$ through thickness.....  | 65 |
| Figure 3.7 - The distribution of $\gamma_{xy}$ through the laminate.....                                   | 66 |
| Figure 3.8 - Moire fringes of glass/epoxy laminates.....   | 68 |
| Figure 3.9 - Distribution of $\epsilon_{xx}$ through laminate thickness .....                              | 69 |
| Figure 3.10 -Distribution of $\epsilon_{yy}$ through thickness.....  | 70 |
| Figure 3.11 - Distribution of $\gamma_{xy}$ through thickness.....   | 71 |

### Chapter 4

|   |    |
|---|----|
| Figure 4.1 - Free body diagrams for: (a) the interface model, and (b) the interphase model..... | 81 |
| Figure 4.2 - Schematic diagram of various joining techniques .....                              | 90 |

|   |     |
|---|-----|
| Figure 4.3 - Schematic diagram of optical setup for moire interferometry (horizontal two beams only) .....  | 94  |
| Figure 4.4 - Moire fringe pattern for: (a) ONE (one laminate beam), (b) 2B (2 for two-laminate and B for bonding), (c) TWO (for two laminates), and (d) 2T (2 for two-laminate and T for taping) .....  | 97  |
| Figure 4.5 - Moire fringe pattern for: (a) 2R2 (the first 2 for two-laminate, R for riveting and the second 2 for two rivets per 50 mm), (b) 2R3 (R for riveting and 3 for three rivets per 50 mm), (c) 2R4 (R for riveting and 4 for four rivets per 50 mm), and (d) 2BR3 (B for bonding, R for riveting and 3 for three rivets per 50 mm) ..... | 99  |
| Figure 4.6.- Moire fringe patterns of various joinig subjected to four point bending: (a) 2S3 (90N) (S for stitching and 3 for three stitches per 50 mm), (b) 2S3 (200 N) , (c) 2S5 (S for stitching and 5 for 5-by-2 stitching pattern), and (d) 2BS3 (B for bonding, S for stitching and 3 for three stitches per 50 mm).....                   | 101 |
| Figure 4.7 - Normal strain calculations, (a) moire fringe pattern for ONE case in five designated locations, (b) relation between u-fringes and $N_x$ in five locations, and (c) strains in the five locations along y-axis .....   | 105 |
| Figure 4.8 - Comparison of normal strain for perfect bonding ONE and imperfect bonding 2B .....   | 107 |
| Figure 4.9 - Schematic diagram for: (a) prefect bonding, (b) imperfect bonding, and (c) no bonding.....   | 108 |
| Figure 4.10 - Comparison between analytical predictions and experimental results ....   | 111 |

## APPENDIX A

|   |     |
|---|-----|
| Figure A.1- Fringe patterns of a notched glass/epoxy beam with PL8 moire-photoelasticity coating (344.72 N) (a) reflection isochromatic fringes, (b) U-displacement fringes, and (c) simultaneous recording of photoelasticity and moire fringes..... | 126 |
| Figure A.2 - Moire Fringe pattern for 67.5 N, (a) 2B, (b) TWO, (c) 2T, and (d) 2R2 .....  | 127 |
| Figure A.3 - Moire fringe patterns (67.5 N) (a) 2R3, (b) 2R4, (c) 2BR3, and (d) 2S3....   | 128 |
| Figure A. 4 - Moire fringe patterns (67.5 N), (a) 2S5, and (b) 2BS3 .....   | 129 |
| Figure A.5 - Moire fringe patterns for graphite/epoxy laminates with three different widths .....   | 130 |
| Figure A.6 - Moire fringes of glass/epoxy laminates at a zero loaf .....  | 131 |

## Chapter 1

### MOIRE INTERFEROMETRY

#### Introduction

When one pattern of repeating lines overlaps with another similar pattern, a third pattern called moire fringe could be created. This phenomenon can be seen in many aspects of daily life. For example, when one looks through a fence towards another fence, a pattern of light and dark lines is composed from the two fences. The meaning of the word *moire* derives from the French word of silk in which the threads form patterns when overlapping one another [1.1]. Figure 1.1 demonstrates two different moire patterns.

When two sets of grating made from straight lines, their superposition will create moire fringe patterns that are straight lines as well. This phenomenon is called geometric moire. In geometric moire, the moire fringes are governed by mathematical equations. The mathematical equations represent displacements that occur due to overlapping of two sets of grating. The direct relationship between the two sets of grating and the moire fringes enables geometrical moire to be used for deformation measurements. However, if the deformation is too small, the geometric moire, due to its low grating frequency, will be unable to measure the deformed displacements.

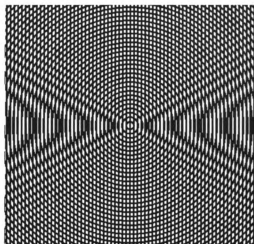
In order to measure small deformations accurately, geometrical moire has been modified by a technique called moire interferometry. Moire interferometry is an optical method that is based on a laser light. In performing moire interferometry, a grating made of furrows with equal spacing must be attached on the surface of a specimen. When the grating is illuminated by two laser beams with specific incident angles, the two beams will be reflectively diffracted from the grating. If the specimen is undeformed, the two beams will be normal to the specimen surface and parallel to each other. If the specimen is deformed, the grating will be altered, and so will be the direction of the diffraction beams. Consequently, the two diffracted beams will interfere with each other and form a set of fringes, i.e. the moire fringes. A good summary of moire interferometry can be found in Post et al. [1.2] and Post [1.3]

## **Background**

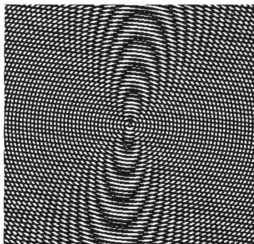
### ***Geometric moire***

Geometric moire, as shown in Figure 1.2, is based on two sets of grating with a relatively low frequency, e.g. 50 lines/mm [1.4-1.6]. One set of grating is strictly attached to the surface of a flat specimen. Another set of grating identical grating is used as reference and is required to create a moire fringe pattern. [1.6]

A moire fringe pattern consists of contour lines of in-plane displacements in the directions normal to the reference grating lines. A recorded fringe pattern



(a)



(b)

Figure 1.1- Moiré fringe patterns from various shapes of patterns overlapping one another

can be are related to in mathematical equations to determine the deformation of a tested specimen. An equation combining displacement and moire fringe is given below:

$$U = \frac{1}{f} N_x \quad (1.1)$$

where U is the displacement in the direction perpendicular to the reference grating lines,  $f$  is the frequency of the reference grating, and N is an integer value assigned for the contour lines and is known as fringe order. Strains of the tested specimen can then be obtained by differentiating Equation (1.1) In the case that the grating lines are normal to the x-axis, the strains in the x-directions should become

$$\varepsilon_x = \frac{1}{f} \frac{\partial N_x}{\partial x}. \quad (1.2)$$

Apparently, the mathematical equation is also dependent on the frequency of the reference grating [1.5]. Geometric moire has been used in, many applications, however, its sensitivity is too low for measurements involving small deformation.

### ***Moire interferometry***

In an effort to increase the sensitivity of displacement measurements, the geometric moire technique was extended to an interferometric technique. This new technique was called moire interferometry. Moire interferometry uses a light



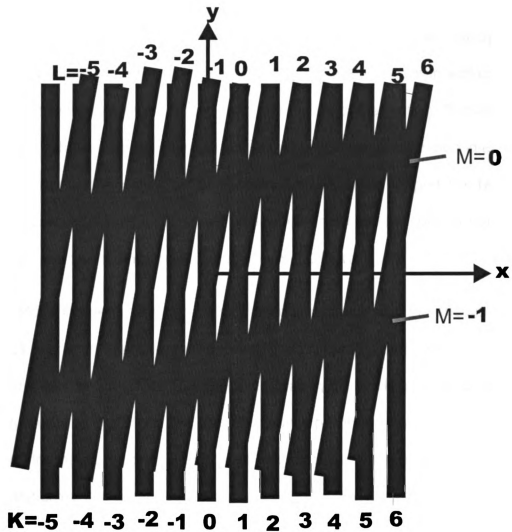


Figure 1.2- Schematic diagram for geometrical moiré formation

source capable of high sensitivity. Moire interferometry is based on the diffraction of two coherent beams from specimen and the interference of the diffracted beams as well. One of the primary elements of moire interferometry is the diffraction specimen grating. When a load is applied to a specimen, the specimen will deform along with the grating that is attached on the specimen surface. This deformation changes the frequency and orientation of the grating. Subsequently, when two coherent light beams illuminate on the deformed specimen in equal but opposite angles, the wave-front of the diffraction becomes warped. The two warped wave-fronts will interfere with one another to create a contour map known as the moire fringe patterns as shown in Figure 1.3.

Moire interferometry can be explained in a casual way that the specimen gratings interferes with a virtual reference grating created by interference of two coherent laser beams [1.2]. The specimen grating is usually of a cross-line grating, meaning that it has two sets of mutually perpendicular grating lines and allowing for measurements in two directions normal to the grating lines. Most often, the cross-line grating is positioned in such a way to measure displacements in the x-direction and the y-direction. Hence, displacements are related to two images (x-displacement fringe pattern and y-displacement fringe pattern) by an expression similar to that of Equation (1.1), i.e.

$$U = \frac{1}{f} N_x, \text{ and } V = \frac{1}{f} N_y \quad (1.3)$$

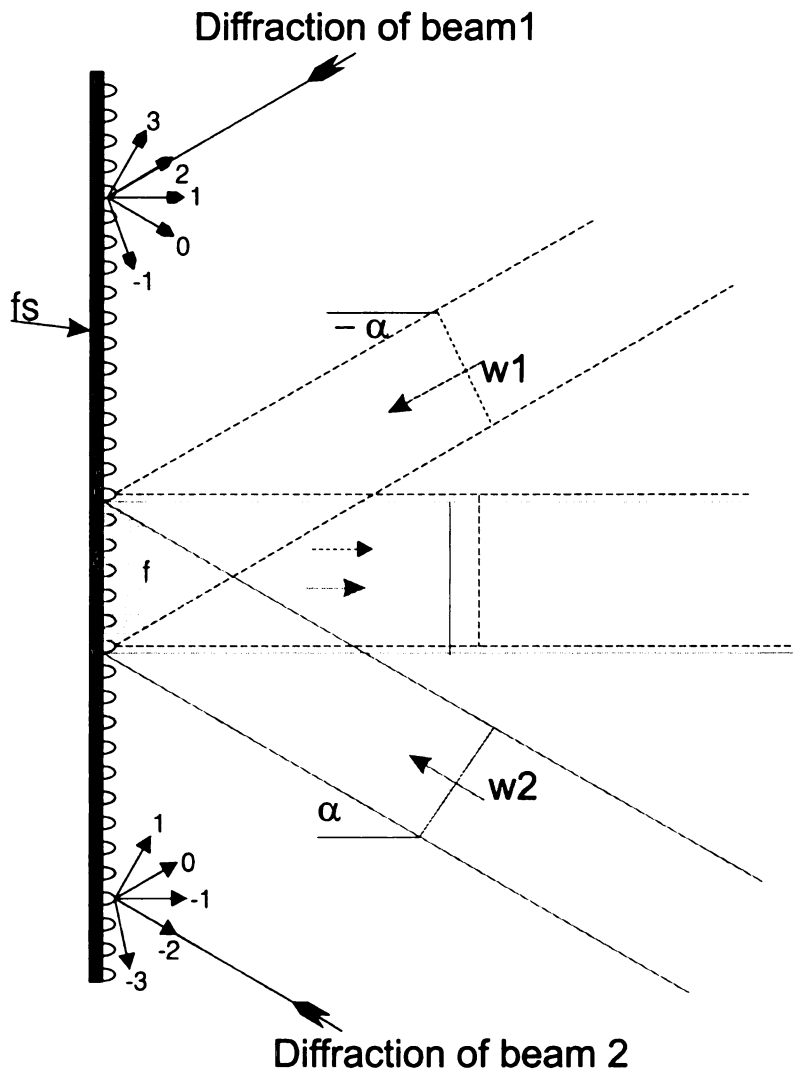


Figure 1.3 - Schematic diagram of moire interferometry

where U, and V are displacements in x and y- axis respectively, and  $N_x$  and  $N_y$  are integer values representing the fringe orders for the U and V, respectively.

The complete two-dimensional strains can then be expressed by combining Equation (1.3) with strain-displacement relations,

$$\begin{aligned}\varepsilon_x &= \frac{\partial U}{\partial x} = \frac{1}{f} \frac{\partial N_x}{\partial x} \\ \varepsilon_y &= \frac{\partial V}{\partial y} = \frac{1}{f} \frac{\partial N_y}{\partial y} \\ \gamma_{xy} &= \frac{\partial U}{\partial y} + \frac{\partial V}{\partial x} = \frac{1}{f} \left[ \frac{\partial N_x}{\partial y} + \frac{\partial N_y}{\partial x} \right]\end{aligned}\tag{1.4}$$

## Literature review

### *Diffraction grating*

The fundamental and essential tool needed for moire interferometry to work is the high frequency diffraction grating. There are two methods of making grating [1.7-1.8]: the direct exposure method onto the specimen and the replication method. In the direct method, a photoresist material is spread on the specimen surface. The specimen is then exposed to an interference patterns formed by two coherent beams for direct grating. In the replication method, a submaster grating is used to transfer the grid onto the specimen surface.

The direct exposure method is applied in a high temperature environment. It is to prepare a high temperature grating [1.9-1.13]. Ifju et al [1.13] coated a

specimen with a film of reflective metal and then applied a photoresist layer. The specimen was then exposed to an interference pattern. Ion etching was then applied to remove the photoresist layer while retaining the grating of the reflective metal. This technique results in a zero thickness grating that can withstand high temperature environments. Cloud et al [1.10] and Kang et al [1.11] created high temperature grating by exposing a photoresist layer to radiation from a mercury light through a submaster grating. Kang et al [1.11] used the same procedures as Cloud et al [1.10], to generate grating except substituting the reflective metal by a special photoresist painting.

The replication method utilizes the following procedures. A layer of photoresist material is applied to a glass substrate and is then exposed to an interference pattern grating to generate a holographic grating. The gratings is then produced via replication, which is well described by Basehore et al. [1.14], Post et al. [1.2], Walker et al. [1.16], and Rowlands et al. [1.17]. The most usable method of replication is presented by Ifju [1.18]. His procedures use the following steps (a) A master grating made of silicone is replicated onto glass substrate using an epoxy resin, the two layers are then separated. (b) Two successive layers of reflective metals separated by Photo-flo (from Eastman Kodak Company) are evaporated on the epoxy grating. The upper layer of the metal is separated and transferred to the specimen by a thin film of epoxy. Guo et al. [1.7] also gave a brief descriptions of replication method.

Boeman [1.20] presented a new technique to replicate grating on semi-cylindrical surfaces and other curved surfaces. By using a flexible substrate he

replicated the deformed grating from the circumference of a hole. The flexible substrate was then be flattened and placed on the interferometer for interference with the virtual reference grating. Mollenhauer [1.20] used a replication technique similar to Boeman's technique, however, instead of flattening the deformed grating from the cylindrical shape, he kept the deformed grating on the circular sector. He then recorded the moire fringe pattern in discrete sections with an increment of five degrees

### ***Applications of moire interferometry***

Moire interferometry has become a widely adopted technique for measuring displacements and hence strains due to its whole-field and high-sensitivity capability. It has many applications in areas ranging from conventional metals to composite materials.

Barbat et al. [1.21] utilized moire interferometry to measure the shear strains along the contact zone between a die and the metallic material. They verified the frictional force and identified the frictional condition. Klein et al. [1.22] measured strains for polymer- based composites subjected to compressive loading. The strains were used to determine the viscoelastic behavior of the composites under compressive loading. Bowles et al. [1.23] investigated moire interferometry in a thermal environment. In their study, Moire was used in high temperature for measuring coefficients of thermal expansion of graphite/epoxy laminates.

Moire and microscopic moire were studied extensively by Han [1.24-1.26] to determine thermal deformation for microelectronic devices. Han introduced a frequency with a higher grating of 4800 lines/mm by passing the laser light through a medium with a higher index of refractions.

McKelvie [1.27] used the technique as a tool to satisfy the boundary condition of a crack due to delamination in multi-layered composites. He used moire interferometry as a tool to calculate the J-Integral in a multi-layered multidirectional composite structure around the tip of crack on a free-edge surface. He then substituted the experimental deformation into a finite element model to find the  $G_I$  and  $G_{II}$ .

An important investigation on the micromechanical behavior of thick-laminated composite was conducted by Post [1.4] and Guo et al [1.29]. Their studies showed that there was a strong free-edge effect when graphite/epoxy was under compression. Molenhauer [1.20] used a grating technique modified from Bemoan [1.19] to measure the strain concentration of around a drilled hole in multi-layered graphite/epoxy composites.

Moire interferometry had been used for measuring surface displacements in structures with complex geometry. As technology advanced, there was a need to integrate results from more measurements with a computational models.

## **Objectives**

The objectives of this research are

- 1. To modify the moire grating technique, which will extend the moire interferometry to more versatile measurements and to obtain more information in each measurement. Effort is centered in reducing the coating layers from the conventional two-layer grating to a modified one-layer grating.**
- 2. To combine the moire interferometry and the photoelasticity technique, which will be capable of presenting both moire and photoelasticity fringe patterns simultaneously. Effort is centered on modifying the moire interferometer to incorporate the polariscopes in two different systems: Transparent photoelasticity, and reflection photoelasticity.**
- 3. To investigate the free-edge effect on distributions of surface strains. This method of high interlaminar shear stresses due to free-edge effect is an important concern in designs of composites laminates. This investigation will also evaluate the feasibility of experimental methods based on surface measurements such as moire interferometry.**
- 4. To explore the joining force of assembled composite beams. Effort is centered on quantifying the joining conditions, both analytical and experimental for different joining techniques. The joining techniques will include various combinations such as adhesive bonding, mechanical riveting, stitching joining and combinations of these techniques. The joining techniques will be considered as alternatives to thick-laminated composite plates.**



## **Organization**

This work is composed of five chapters: Chapter one is an introduction, which describes briefly the historical background, and the objectives of the research. Chapter two deals first with modifying the moire grating, and second with combining moire interferometry and photoelasticity. Chapter three investigates the mismatch of materials properties and the free edge effect on distributions of surface strains. Chapter four focuses on the joining forces in assembled composite beams. Chapter five draws the conclusions from the studies presented.

## References

- 1.1 Walker, C. "A Historical Review of Moire Interferometry" *Experimental Mechanics*, 281-299, (December 1994).
- 1.2 Post, D., Han, B., and Ifju, P., *High Sensitivity Moire*, Springer-Verlag, 1993
- 1.3 Post, D. "Chapter 7, Moire Interferometry" *Handbook on Experimental Mechanics, Second Edition*, Edited by Kobayashi, A, SEM press, 297-329,1993.
- 1.4 Cloud, G., "Optical methods of engineering analysis," Cambridge University Press 1995.
- 1.5 Parks, V, "Chapter 6, Geometric Moire" *Handbook on Experimental Mechanics, Second Edition*, Edited by Kobayashi, A, SEM press, 267-296,1993.
- 1.6 Sciammarella, C., "The Moire Method - A Review" *Experimental Mechanics*, 418-433, November 1982
- 1.7 Guo, Y., Ifju, P., Boeman, R., and Dai, F., "Formation of Specimen Grating for Moire Interferometry Applications," *Experimental Techniques*, 28-32, (September/October 1999.)
- 1.8 Guo, Y., Ifju, P., Boeman, R., and Dai, F., "Formation of Specimen Grating for Moire Interferometry Applications," *Abstracts Proceeding of SEM Spring Conference*, 291-292, Bellevue, WA, (June 1997.)
- 1.9 Huimin, P., Dietz, P., Fulong D. and Schmid, A., "Fabrication of High Temperatures Grating for High Temperature," *Experimental Techniques*, 28-29, (September/October 1995.)
- 1.10 Cloud, G., Radake, R. and Peiffer, J., "Moire Grating for High Temperatures and Long Times," *Experimental Mechanics*, 19 (10), 1-3, (October 1979.)
- 1.11 Kang, B., Zhang, G., Jenkins, M., Ferber, M., Ifju, P., "Development of Moire Interferometry for In Situ Material Surface Deformation Measurement At High Temperature," *proceedings of the ATEM 93 Conference on Advanced Conference on Advanced Technology in Experimental Mechanics*, Kanazawa, Japan, 964-976, (August, 1993.)
- 1.12 Guo, Y., Chen, W., and Lim, K., "Experimental Determinations of Thermal

**Strains in Semiconductor Packaging Using Moire interferometry,"  
Advances in Electronic Packaging, ASME, 779-784, (1992.)**

- 1.13 Ifju, P., Post, D., "Zero-Thickness Specimen Grating For Moire Interferometry," Experimental Techniques, 45-47, (March/April 1991.)**
- 1.14 Basehore, M. and Post, D., "High-frequency, High-reflectance Transferable Moire Gratings," Experimental Techniques, 29-31 (May 1984.)**
- 1.15 Rowalds, R.,Vallem, J., "On Replication for Moire-Fringe Multiplication," Experimental Mechanics, 167-169, (May 1980.)**
- 1.16 Walker, C., and Mcklevie, J., "A Practical Multiplied-Moire System," Experimental Mechanics, 316-320, (August 1978.)**
- 1.17 Rowalds, R.,Vallem, J., "On Replication for Moire-Fringe Multiplication," Experimental Mechanics, 167-169, (May 1980.)**
- 1.18 Ifju, P, "Replication of Master Grating," Special report.**
- 1.19 Boeman, R. "Interlaminar Strains at The Free-Edge of a Hole for Thick Composites in Compression," Proceeding of SEM Spring Conference Milwaukee, Wisconsin, 203-315, June 1991.**
- 1.20 Mollenhauer, D. " Interlaminar Deformation at Hole in Laminated Composites: A detailed Experimental Investigation Using Moire Interferometry," Ph.D. Dissertation, Virginia Polytechnic Institute and State University, Blacksburg, VA, August 1997.**
- 1.21 Barbat, S., "Metal-Forming studies By Moire Interferometry," Experimental Techniques, 25-28, (June 1989.)**
- 1.22 Klien, R.,Tuttle, M., "Strain Measurements In Composites Subjected To Compressive Loading Using Moire Interferometry," Proceeding of SEM Spring Conference Huston, Texas, 649-656, June 1987.**
- 1.23 Bowels, D. and Post, D., and Herakovich, C. T., and Tenney, D., R." Moire Interferometry for Thermal Expansion of Composites," Experimental Mechanics, 441-447, (December 1981.)**
- 1.24 Han, B, "Higher Sensitivity Moire Interferometry for Micromechanics Studies," Optical Engineering, Vol. 31, No7, 1517-1526, (1992.)**
- 1.25 Han, B. "Extension of Moire Interferometry Into The Ultra-High Sensitivity Domain", Ph.D. Dissertation, Virginia Polytechnic Institute and State**

University, Blacksburg, VA, March 1991.

- 1.26 Han, B., "Recent Advancements of Moire and Microscopic Moire Interferometry for Thermal Deformation Analysis of Microelectronic Devices," *Experimental Mechanics*, 278-288, (December 1998.)
- 1.27 Mcklevie, J., and Perry, K." Moire Interferometry as a Detailed Validator for Computational modeling of Composites," *Composite Structures*, 299-305, (1998).
- 1.28 Guo, Y., Post, D., and Han, B. "Thick Composite in Compression: Micromechanical Behavior and Smeared Engineering Properties," *Journal of Composite Materials*, Vol. 26, No. 13, 1930-1944, (1992)

## Chapter 2

### COMBINING MOIRE INTERFEROMETRY AND PHOTOELASTICITY

#### **Abstract**

Both moire interferometry and photoelasticity have been used for stress analysis of composite structures. In this study, polariscopes were incorporated into a moire interferometer to form a system capable of presenting both moire and photoelasticity fringe patterns. However, obtaining both types of fringe patterns simultaneously requires a transparent moire grating and a reflection photoelasticity coating (also transparent) on the surface of a testing specimen. In this study, an epoxy material named PL8 commonly used for photoelasticity coating was used for both purposes. In other words, both the moire grating and reflection photoelasticity coating were made of the same epoxy material and molded simultaneously. In order to develop such a one-layer grating technique for two different types of measurement, a systematic study was conducted on reduction of the layer number of coating from conventional two-layer grating to a modified one-layer. To verify the feasibility of the new grating technique, a glass/epoxy specimen was coated with the single-layer moire-photoelasticity grating. A hole was prepared at the center of the specimen, which was then subjected to four-point bending. Strain distributions obtained from moire interferometry and reflection photoelasticity were found to have a fair agreement with those from finite element analysis.

## Introduction

Due to its high accuracy and high sensitivity, moire interferometry has been commonly used in both macroscopic and microscopic strain measurements. Many applications can be found in the literature [2.2-2.18]. Details of the technique for moire interferometry has been well summarized in a book authored by Post, Han, and Ifju [2.19]. Figure 2.1 shows one of the common setups of moire interferometry. It is also the fundamental setup used in the present study.

As shown in Figure 2.1, the point laser beam is diverged through a spatial filter and then redirected and collimated by a parabolic mirror. The enlarged collimated light is then illuminated onto four mirrors (M) located in the moire interferometer. For reasons of clarity, only the two horizontal ones (the right and the left) are shown in the figure. The light beams reflected from these four mirrors are directed onto another four mirrors for further beam angle adjustment. (Again, only the two horizontal mirrors are shown in the diagram.) The moire interferometry is based on optical diffraction and interference. As the two beams (e.g. the right and the left) are emitted from the second set of mirrors, the beams are reflectively diffracted by the moire grating on the testing specimen. Under a no-loading condition, the two diffracted beams should point in the direction normal to the specimen surface and cause no interference between them. However, if the specimen is deformed due to external loading, the pitch of moire grating will be altered. And the diffracted beams will no longer be

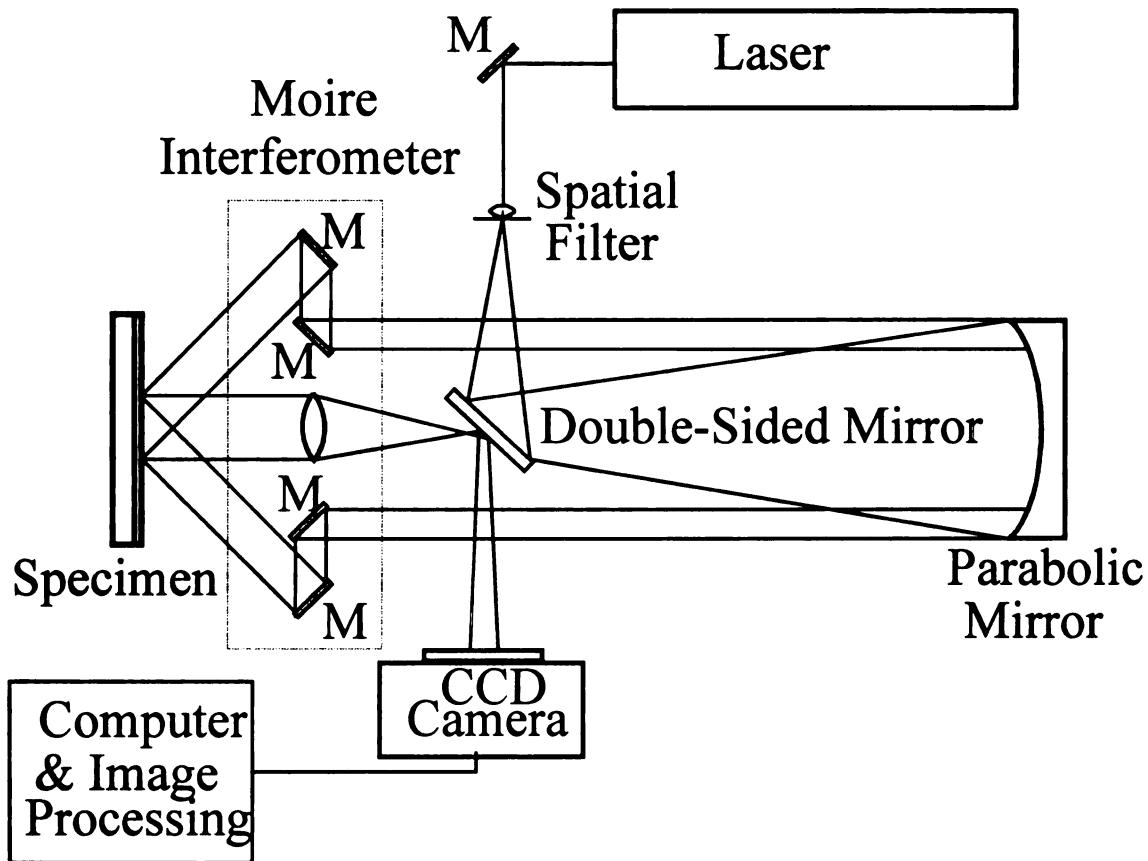


Figure 2.1- Schematic diagram of optical setup for moire interferometry (horizontal two beams only).

parallel to each other and normal to the specimen surface. Interference between the beams will then take place and form a moire fringe pattern representing the contours of constant displacement. The two horizontal beams (the right and the left) can give horizontal displacement (U-displacement) contours while the two vertical beams (not shown in the diagram) gives vertical displacement (V-displacement) contours. The deformation of the specimen can be calculated from the contours (moire fringe patterns).

The objectives of the present study is to extend moire interferometry to more versatile measurements and to obtain more information in each measurement, possible modifications in both grating technique and the optical setup need to be explored.

## **Grating techniques**

### ***Two-layer grating***

#### **Conventional technique**

In addition to the moire interferometer and optic setup in Figure 2.1, another important element of moire interferometry is moire grating. As a conventional practice [2.6], the preparation of moire grating for a testing specimen can be achieved by the following procedures. First of all, a mother grating made of epoxy is required. A layer of aluminum is then coated on the surface of the mother grating. The aluminum layer is then transferred onto a testing specimen via a sticky coating layer of epoxy on the specimen surface.



Once the epoxy layer is cured, there exist two layers, epoxy and aluminum, on the specimen. The technique is then called two-layer grating technique.

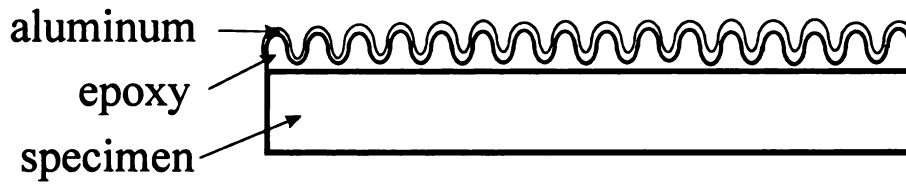
### **Modified technique**

Many studies aiming at improving the moire grating can be found in the literature [2.14-2.19]. The following procedures for grating preparation were developed in the present study. Instead of the epoxy mother grating used in the conventional technique, the present technique started from a mother grating made of silicon rubber. An epoxy was then spin-coated on the surface of the silicon rubber grating. In addition to duplicity the moire grating, the epoxy layer was also used as a bonding medium to transfer the grating onto a testing specimen. Once the epoxy is cured, it can be coated with aluminum to enhance the capability optical reflection.

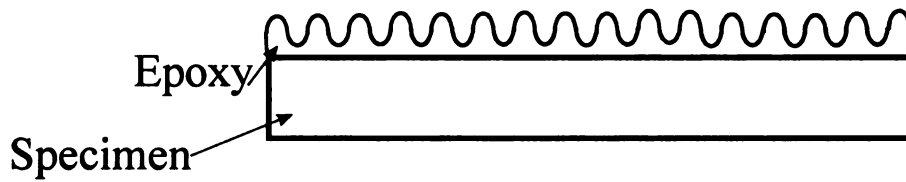
Figure 2.2(a) shows the schematic diagram of a specimen with two-layer grating for both the conventional and simplified techniques. In an effort to further simplify the grating technique but retain good quality of moire fringe pattern for strain analysis, a few studies listed below were explored.

### ***One-layer grating***

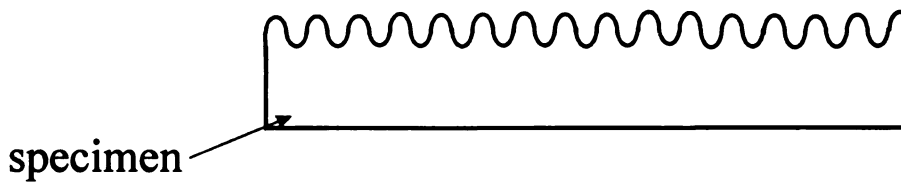
In an effort to reduce the number of layers, the aluminum coating layer was omitted from the two-layer grating technique, resulting in one-layer grating, i.e. epoxy layer only as shown in Figure 2. 2(b) schematically. It was expected



(a)



(b)



(c)

Figure 2.2- Schematic diagrams of specimen with (a) two-layer grating, (b) one-layer grating, and (c) zero-layer grating

that the optical reflection would be hindered up to some extent. In order to investigate the effects of aluminum coating on the image enhancement, the following studies representing specimens with different degrees of reflection were performed:

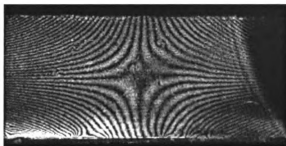
- A. **Black Specimen** – In this study, an aluminum specimen with dimensions of 100 mm x 12.5 mm x 3 mm was coated with a layer of black paint. An epoxy layer was then spin-coated on the surface of the black paint layer before being printed with moire grating.
- B. **White Specimen** – Instead of the black paint mentioned in A, a layer of white paint was coated on the surface of the aluminum specimen before the epoxy-grating layer was introduced to the specimen.
- C. **Bright Specimen** – The aluminum specimen was polished carefully to have a very smooth and shining surface before being coated with the epoxy grating.
- D. **Transparent Specimen** – Instead of aluminum specimen, a photoelasticity sensitive material PSM-5A, was coated with epoxy grating, which is also transparent.

These four specimens represented four different degrees of reflection. The bright specimen gave the best reflection followed by the white specimen, which had better reflection than the black specimen. Being transparent, the specimen had the lowest capability of reflection.

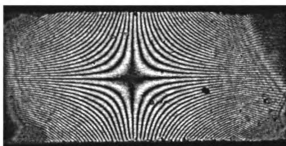
All four specimens were loaded by four-point bending. Experimental results of the two extreme cases of reflection, C and D, are shown in Figures 2.3(a) and 2.3(b), respectively. (The image from specimen C was specially prepared by using a filter to reduce the strength of the shining background.) Apparently, both specimens show details of moire fringe patterns. And, in fact, by adjusting the light intensity and exposure time, it was possible to obtain images with similar quality. In other words, It was possible to obtain good quality of fringe pattern with less efforts without using the aluminum coating layer.

### ***Zero-layer grating***

To further reduce the number of grating layers, a technique called zero-layer grating was developed. In fact, first of all, a silicon rubber mold was built for casting the epoxy specimen. The mold was essentially a container for accommodating liquid polymer. In order to cast an epoxy specimen with moire grating on its surface in one single process, an aluminum specimen having the same in-plane dimensions as the specimen-to-be was coated with a silicone rubber moire grating on the surface and the specimen was fixed at the bottom of the silicon rubber mold. The thickness of the aluminum specimen was chosen so that the remaining height of the silicon rubber mold was equal to the thickness of the specimen-to-be. A liquid epoxy was then poured into the mold. And a dead



(a)



(b)

Figure 2. 3 - U-displacement moire fringe patterns from four-point bend tests for (a) polished aluminum specimen and (b) transparent PSM-5A specimen

weight was placed on top of the liquid polymer. Figure 2.4 shows the schematic diagram of the processing setup. Once the epoxy specimen was cured, it could be popped out easily due to the use of silicon rubber as the mold. Since both the specimen and the coating were made of the same material and formed simultaneously, i.e. there was no independent layer for grating, this type of specimen was called no-layer grating. A schematic diagram for no-layer grating is shown in Figure 2.2(c).

## **Combining moire and photoelasticity**

### ***Transmission photoelasticity***

Applying four-point bending to the specimen of no-layer grating resulted in high quality moire fringe patterns. In addition, since the specimen was made of high-sensitivity photoelasticity material PSM-5A, clear transmission photoelasticity fringes could be obtained by adding a polarizer and an analyzer to the existing moire interferometry system. Figure 2.5 shows the schematic diagram of the experimental setup. The dotted lines are used in the diagram to enhance the optical path for photoelasticity investigation whereas the solid lines for moire interferometry. Figures 2.6(a), 2.6(b) and 2.6(c) show the results of photoelasticity fringe pattern (isochromatic), moire fringe pattern (U-displacement) and the simultaneous recording of the two, respectively.

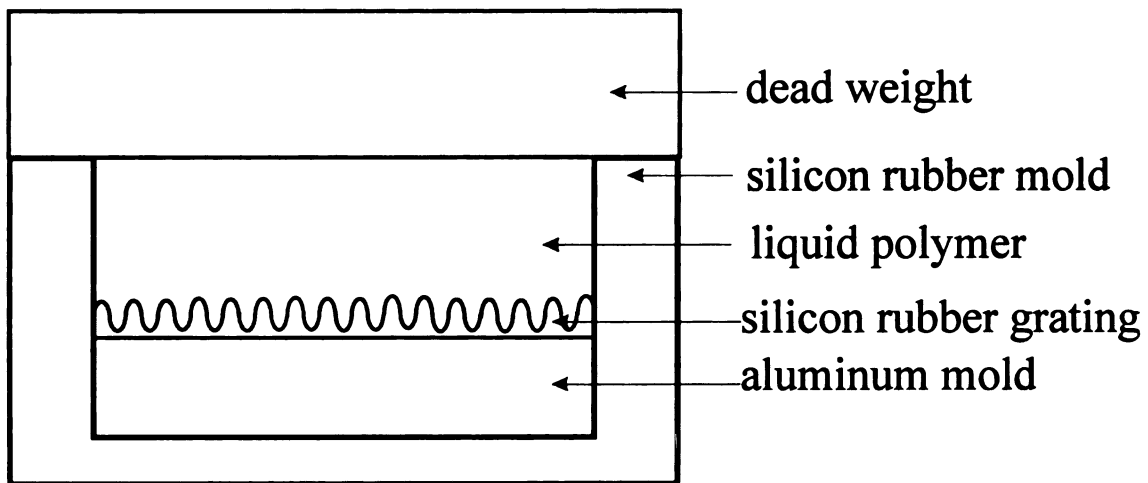


Figure 2. 4 - Schematic diagram of processing setup for casting a specimen with zero-layer grating.

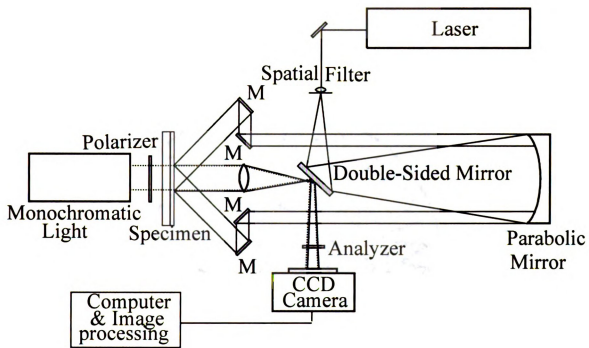


Figure 2.5 - Schematic diagram of optical setup for combining moiré interferometry and transmission photoelasticity.

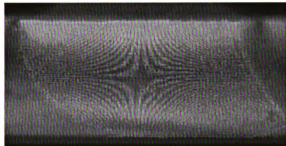




(a)



(b)



(c)

Figure 2.6 - Fringe patterns of PSM-5A beam under four-point bending: (a) transmission isochromatic fringes, (b) U-displacement fringes, and (c) simultaneous recording of photoelasticity and moire fringes

## ***Reflection photoelasticity***

Transmission photoelasticity can present high-quality isochromatic fringe patterns and has been commonly used in engineering applications.

Unfortunately, most engineering materials are opaque or have low sensitivity of photoelasticity phenomenon. Hence, it is necessary to use the technique of reflection photoelasticity for those materials [2.20-2.22]. Reflection photoelasticity fringe pattern could be obtained by coating the PSM-5A specimen of one-layer grating with a reflective material, such as gold, on the surface opposite to that having moire grating. A few setups were explored. Figure 2.7 shows the position of the polarizer and analyzer of the experimental setup found to be the most convenient and gave the highest quality of image among the techniques explored. The dotted lines again show the optical path of the photoelasticity investigation. Experimental results of photoelasticity fringe pattern (isochromatic), moire fringe pattern (U-displacement), and the combination of the two fringe patterns are given in Figures 2.8(a), 2.8(b), and 2.8(c), respectively.

## ***Single coating for both moire and photoelasticity***

The technique combining moire interferometry and reflection photoelasticity can be applied to both transparent and opaque specimens. In order to simplify the technique requiring two sets of coating, a single coating technique was developed for both moire interferometry and reflection photoelasticity. A procedure similar to casting zero-layer grating was followed, in casting the single moire-photoelasticity coating. Firstly, an aluminum specimen

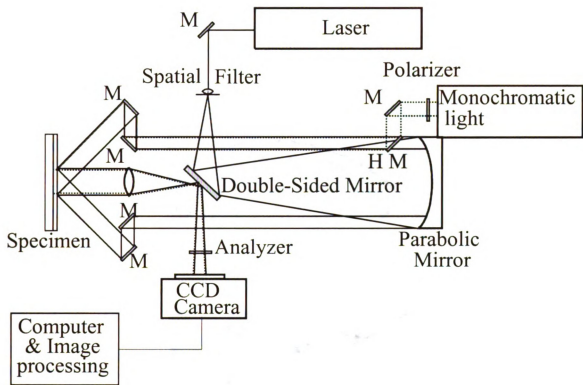
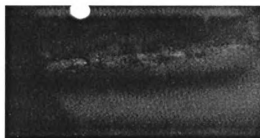
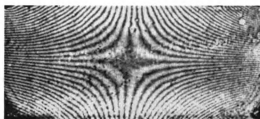


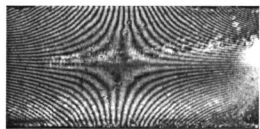
Figure 2.7 - Schematic diagram of optical setup for combining moiré interferometry and reflection photoelasticity.



(a)



(b)



(c)

Figure 2.8 - Fringe patterns of a PSM-5A beam under four point bending: (a) reflection isochromatic fringes, (b) U-displacement fringes, and (c) simultaneous recording of photoelasticity and moire fringes.

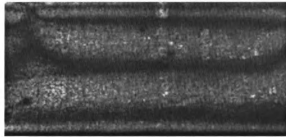
having the same in-plane dimensions as the mold and coated with silicon rubber moire grating was fixed at the bottom of the silicon rubber mold as shown in Figure 2.4. Liquid epoxy PL8 was then poured into the mold until the height was equal to the desired thickness. The testing specimen, followed by dead weight, was then placed on the surface of the liquid epoxy. The entire setup was left for curing at room temperature for about 24 hours.

A glass/epoxy specimen coated with the PL8 moire-photoelasticity layer was prepared and subjected to four-point bending. Results of the photoelasticity fringe pattern, moire fringe pattern, and the simultaneous recording of the two patterns are given in Figure 2.9(a), 2.9 (b), and 2.9(c), respectively.

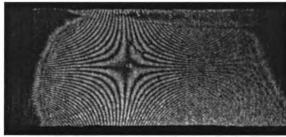
## **Case studies**

### ***Effects of coating thickness***

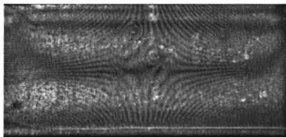
Glass/epoxy specimens with thickness of 6.4 mm were used in the study. In order to investigate the thickness effects of the moire-photoelasticity coating on the measurements for both moire and photoelasticity fringes, three thickness of coating were prepared in the study. They were 0.55 mm, 1.36 mm and 3.17 mm. In order to prepare the 1.36 mm and 3.17 mm coatings, two silicon molds of different thickness were fabricated; whereas the 0.55 mm coating was prepared via the technique of one-layer grating. Figures 2.10(a), 2.10(b) and 2.10(c) show the moire fringe patterns of the three specimens subjected to four point bending.



(a)

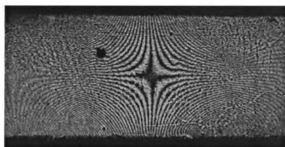


(b)

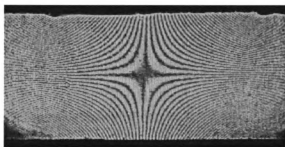


(c)

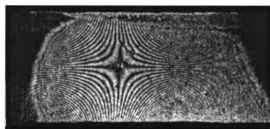
Figure 2.9 - Fringe patterns of a glass/epoxy beam with PL8 moire photoelasticity coating (a) reflection isochromatic fringes, (b) U-displacement fringes, and (c) simultaneous recording of photoelasticity and moire fringes.



(a)



(b)



(c)

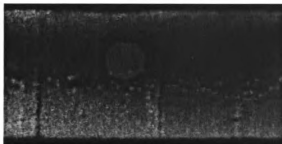
Figure 2.10 - Moire fringe patterns of glass/epoxy beams with PL8 grating thickness of (a) 0.55 mm, (b) 1.36 mm, and (c) 3.17 mm

Apparently, the differences among the three moire fringe patterns are not significant, indicating the good bonding between the coatings and the specimens. The moire fringe patterns also imply the effect of coating reinforcement on specimen deformation. However, due to the fact that the sensitivity of a photoelasticity coating is proportional to its thickness, the 3.17 mm coating gave a denser and sharper fringe pattern than the 1.36 mm one under the same loading condition. Figures 2.11(a), 2.11(b) and 2.11(c) show the testing results. Apparently, the 3.17 mm case has the highest photoelasticity fringe density and is suitable for further stress analysis.

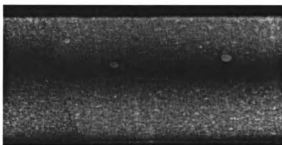
### ***Stress concentration***

In order to evaluate the feasibility of using the combined technique to common stress analysis, an aluminum beam with dimensions of 100 mm x 12.5 mm x 6.4 mm was coated with a moire-photoelasticity layer of 3.17 mm. A hole of 3mm in diameter was introduced to the center of the specimen by a drilling process of 300 rpm and using water as coolant. The specimen was then loaded in a four point bending fixture. Figures 2.12(a) and 2.12(b), and 2.12(c) show photoelasticity, moire and combined fringe patterns, respectively. In addition, a finite element analysis Figure 2.13 based on ABAQUS was performed to compare the experimental results. Figure 2.14 shows the experimental results and numerical simulations of the bending strain distributions along the line across the hole center (shown by the dotted line). Note that because of the low photoelasticity sensitivity of the coating, the results from the reflection

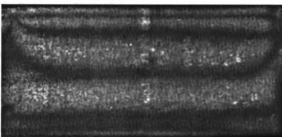




(a)

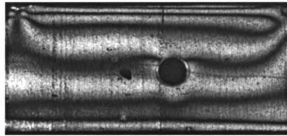


(b)

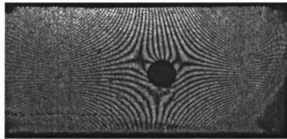


(c)

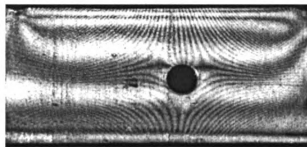
Figure 2.11 - Photoelasticity fringe patterns of glass/epoxy beams with PL8 grating thickness of (a) 0.55 mm (b) 1.36 mm, and (c) 3.17 mm



(a)



(b)



(c)

Figure 2.12 - Fringe patterns of a notched glass/epoxy beam with PL8 moiré-photoelasticity coating (a) reflection isochromatic fringes, (b) U -displacement fringes, and (c) simultaneous recording of photoelasticity and moiré fringes

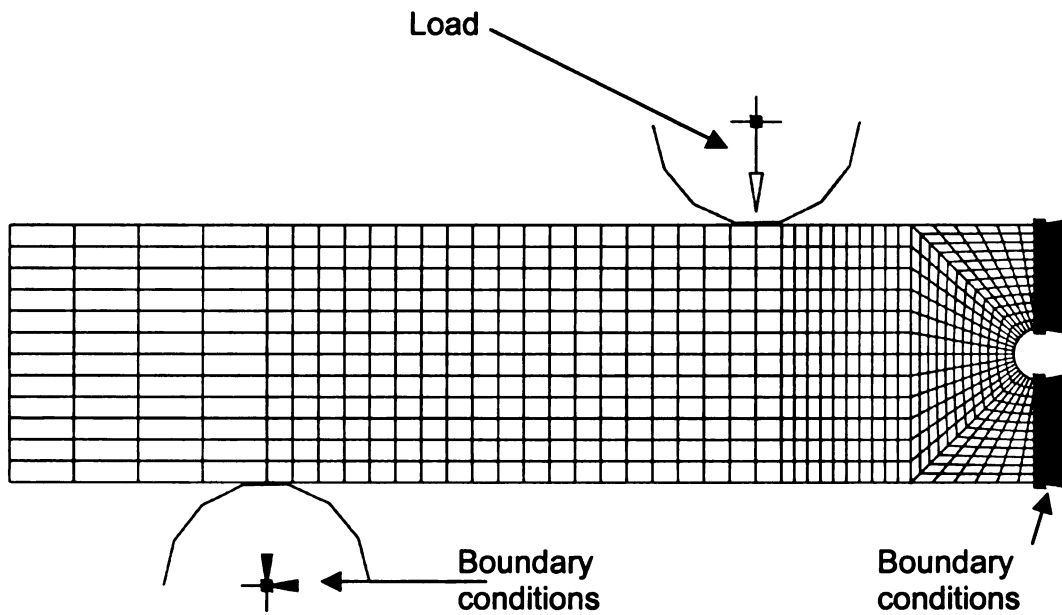


Figure 2.13 - Schematic diagram of finite element model for the beam with central hole; it has 1482 elements, the element type is 8 node element of CPS8R,

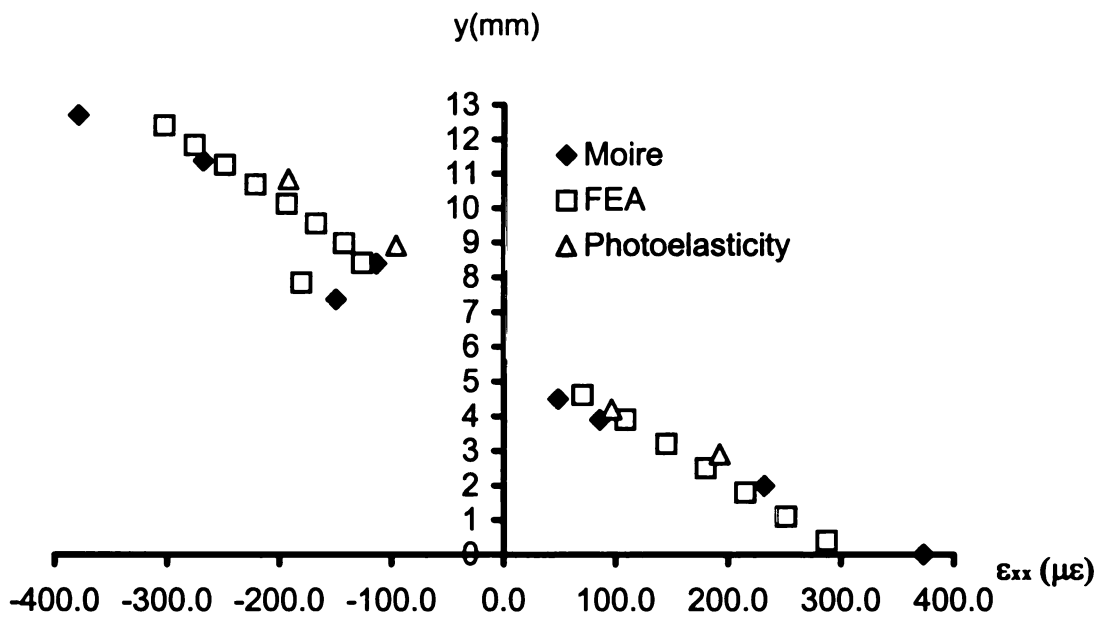
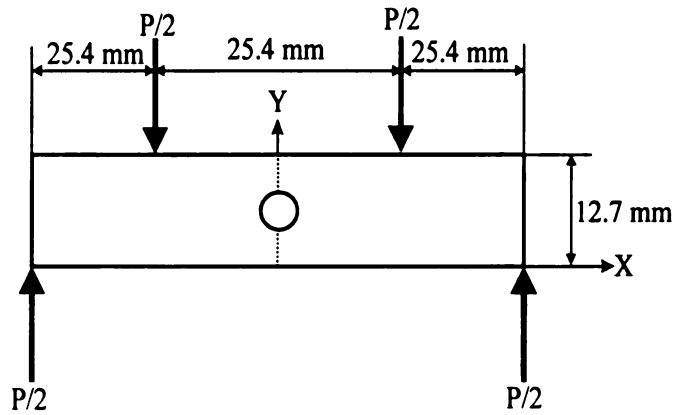


Figure 2.14 - Comparisons of results from moire interferometry, photoelasticity, and finite element analysis.

photoelasticity are not as detailed as the moire counterpart. And the results based on all three techniques seem to agree with one another fairly.

## **Summary**

Based on the experimental results and stress analysis, the following conclusions can be drawn:

A simplified two-layer grating technique was developed. Two-layer grating could be further simplified to one-layer grating by simply omitting the enhancing layer, i.e. aluminum layer. The one-layer grating technique was found to be feasible for moire measurements.

It was worthwhile to develop the technique of no-layer grating since the “layer” did not have thickness; neither was there mismatch of material properties between the specimen and the “layer.”

The technique combining moire and photoelasticity together was capable of presenting two independent sets of experiment and result. It provides a self-verification capability or double-check system.

## **Acknowledgements**

The author wishes to express his sincere thanks to Professor Daniel Post of Virginia Tech for designing the moire interferometer, Professor Peter Ifju of

University of Florida for providing the master moire grating, and Professor Andre Lee of Michigan State University for valuable discussions on spin coating.

## References

- 2.1 Liu, D., Shakour, E." Combining Moire Interferometry and Photoelasticity" Submitted to Experimental Mechanics.
- 2.2 Basehore, M. and Post, D., "High-frequency, High-reflectance Transferable Moire Gratings," Experimental Techniques, 29-31 (May 1984).
- 2.3 Ifju, P.,Kilday, B.,Niu, X., "Residual Stress Measurements in AS4/350-6 Laminates," Abstract Proceedings of SEM Spring Conference, 337-338, Bellevue, WA, (June 1997).
- 2.4 Bowels, D. and Post, D., and Herakovich, C. T., and Tenney, D., R." Moire Interferometry for Thermal Expansion of Composites," Experimental Mechanics, 441-447, (December 1981).
- 2.5 Ifju, P.," The Shear Gage: For Reliable Shear Modulus Measurements of Composite Materials," Experimental Mechanics, 369-378, (December 1994).
- 2.6 Czarnek, R., Post, D., "Strain Concentration Factors in Composite Tensile Members with Central Holes," Proceedings of the 1987 SEM Spring Conference on Experimental Mechanics, Houston, TX, 657-663,(June 1987).
- 2.7 Czarnek, R., and Guo, Y. " Surface Contouring Using Virtual Grating," Experimental Techniques, 35-37, (May/June 1991).
- 2.8 Bradley, D., Adams, D., Gascoigne" Interlaminar Strains and Compressive Strength Reductions Due to Nested Layer Waviness in Composite Laminates," Journal of Reinforced Plastics and Composites, 17 (11), 989-1011, 1998.
- 2.9 Shaw, M., "The Effects of Strength Probabilistics on Fracture Mode of Ceramic/metal Multilayers", Engineering of Fracture Mechanics, 61, 49-74, 1998.
- 2.10 Huimin, P., Dietz, P., Fulong D. and Schmid, A.," Fabrication of High Temperatures Grating for High Temperature, "Experimental Techniques, 28-29, (September/October 1995).
- 2.11 Cloud, G., Radake, R. and Peiffer, J., "Moire Grating for High Temperatures and Long Times," Experimental Mechanics, 19 (10), 1-3, (October 1979).

- 2.12 Kang, B., Zhang, G., Jenkins, M., Ferber, M., Ifju, P., "Development of Moire Interferometry for In Situ Material Surface Deformation Measurement At High Temperature," proceedings of the ATEM 93 Conference on Advanced Conference on Advanced Technology in Experimental Mechanics, Kanazawa, Japan, 964-976, (August, 1993).
- 2.13 Guo, Y., Chen, W., and Lim, K., "Experimental Determinations of Thermal Strains in Semiconductor Packaging Using Moire interferometry," Advances in Electronic Packaging, ASME, 779-784, (1992).
- 2.14 Guo, Y., Ifju, P., Boeman, R., and Dai, F., "Formation of Specimen Grating for Moire Interferometry Applications," Abstracts Proceeding of SEM Spring Conference, 291-292, Bellevue, WA, (June 1997).
- 2.15 Walker, C., and Mcklevie, J., "A Practical Multiplied-Moire System," Experimental Mechanics, 316-320, (August 1978).
- 2.16 Ifju, P., Post, D., "Zero-Thickness Specimen Grating For Moire Interferometry," Experimental Techniques, 45-47, (March/April 1991).
- 2.17 Rowalds, R., Vallem, J., "On Replication for Moire-Fringe Multiplication," Experimental Mechanics, 167-169, (May 1980).
- 2.18 Post, D., Han, B., and Ifju, P., High Sensitivity Moire, Springer-Verlag, 1993.
- 2.19 Cloud, G., "Optical methods of engineering analysis," Cambridge University Press, 1995.
- 2.20 Hung, Y., and Pottinger, M., "An Improved Oblique-incidence technique for Principal-strain Separation in Photoelastic Coating," Experimental Mechanics, 55-63, (February 1962).
- 2.21 Zandman, F., Render, S., and Riegner, E., "Reinforcing Effect of Birefringent Coating," Experimental Mechanics, 55-63, (February 1962).
- 2.22 Theocaris, P., and Dafermos, K. "A Critical Review on the Thickens Effect of Birefringent Coating," Experimental Mechanics, 271-276, (September 1964).
- 2.23 Zandman, F., and Post, D., "Photoelastic-coating Analysis in thermal Fields," Experimental Mechanics, 215-221, (September 1963).
- 2.24 Daniel, M., Rowards, R., and Post, D. "Strain Analysis of Composite by Moire Methods," Experimental Mechanics, 246-252, (June 1973).



- 2.25 Pipes, B. "Interlaminar Stresses in Composite Laminates Under Uniform Axial Extension," *Journal of Composite Materials*, Vol. 4, 538-459, (October 1970).
- 2.26 Han, B., and Post, D., "Immersion Interferometer for Microscopic Moire Interferometry," *Experimental Mechanics*, 38-41, (March 1992).
- 2.27 Han, B., "Recent Advances of Moire and Microscopic Moire Interferometry for Thermal Deformation Analyses of Microelectronic Devices," *Experimental Mechanics*, 278-288, (December 1998).

## **Chapter 3**

### **MISMATCH OF MATERIAL PROPERTIES AND FREE-EDGE EFFECT**

#### **Abstract**

The free-edge effect is a unique and important phenomenon in composite laminates because it could cause high interlaminar stresses on laminate interfaces along free edges and eventually would result in delamination in composite laminates. This study investigated the free-edge effect in graphite/epoxy and glass/epoxy laminates. Moire interferometry was used in the investigations. Experimental results revealed that the shear strains on free edges increased as the width of a composite laminate decreased. However, the normal strains on free edges were not affected by the width change. In addition, the depth of boundary layer was found to be greater than the laminate thickness, especially in the graphite/epoxy laminate, as usually assumed. The free-edge effect, in fact, was associated with mismatch of material properties. Since graphite/epoxy had higher anisotropy than glass/epoxy, it experienced a stronger free-edge effect than the glass/epoxy counterpart. Similarly, a composite laminate consisting of thicker laminae had a higher influence from free edges than that consisting of thinner laminae.

## Free-edge effect

Fiber-reinforced polymer-matrix composites are excellent materials for high-performance structures. They are usually used in thin-laminate form because their properties in the plane of laminates can be excellent. However, their properties in the thickness direction of laminates are not outstanding because composite laminates are weakly bonded by matrix through the thickness. In addition to the poor bonding strength, sudden changes of material properties across laminate interfaces also pose a serious concern on laminate strength. The sudden changes of material properties could be due to different fiber orientations or different material types across the laminate interfaces.

When a composite laminate is subjected to loading, some stress components on the laminate interfaces, so-called interlaminar stresses, could become tremendously large due to sudden changes of material properties across the laminate interfaces. As a result of the high interlaminar stresses and the low interlaminar strengths mentioned earlier, the composite laminate might be damaged along the laminate interfaces, so-called delamination.

The onset of delamination of a composite laminate subjected to uniaxial tension always starts from free edges of the composite laminate. This is because the highest interlaminar stresses are located on laminate interfaces along the free edges. The phenomenon of high interlaminar stresses associated with free edges is a unique phenomenon in composite laminates and is called *free-edge effect*.

Free-edge effect has been well investigated analytically [3.1-3.10]. There are essentially two major modes of free-edge effect; one is concerning the interlaminar shear stress  $\tau_{xz}$  ( $x$  and  $y$  are in-plane coordinates while  $z$  is thickness coordinate) in angle-ply laminates and the other is the interlaminar normal stress  $\sigma_{zz}$  in cross-ply laminates. When an angle-ply laminate, such as  $[+\theta/-\theta]_s$ , is subjected to uniaxial tension, the interface between the  $+\theta$ -lamina and the  $-\theta$ -lamina will have high interlaminar shear stress  $\tau_{xz}$  because of the opposite tension-shearing effects between the two laminae. Similarly, when a cross-ply laminate, such as  $[0/90]_s$ , is subjected to uniaxial tension, the interface between the 0-lamina and the 90-lamina will have high interlaminar normal stress  $\sigma_{zz}$  because of the different Poisson's ratios between the two laminae.

The free-edge effect can cause high interlaminar stresses (both shear and normal), which are important concerns in composite laminate designs. It is also critically important to the evaluations of experimental methods based on surface measurements, e.g. moire, holography, speckle interferometry, etc. The objectives of this study are

1. to investigate the free-edge effect on distributions of surface strains and
2. to evaluate the feasibility of using moire interferometry for two-dimensional analysis of composite laminates.

## **Moire interferometry**

Owing to its high sensitivity, moire interferometry has been commonly used in investigations of composite laminates. Like many other optical methods, moire interferometry is a surface technique. A moire grating (lines with periodic spacing) should be coated on the interested surface of a testing specimen for moire investigations. When the grating is illuminated by two laser beams with special incident angles, the two beams will be reflectively diffracted from the grating, normal to the specimen surface and parallel to each other. As a result, there is no interference between them and an image of no fringe, so-called null field, should be obtained. However, when the specimen is subjected to loading, the spacing among the grating lines will be altered, so will be the directions of the diffracted beams. Consequently, the two beams will interfere each other and form a set of fringes, so-called moire fringes.

The moire fringe pattern resulting from the interference of the two diffracted beams is actually a pattern of contours representing constant levels of displacement in the direction normal to the grating lines. In order to obtain constant levels of displacement in another direction, another two laser beams should be used along with a moire grating with lines normal to that direction. Hence, combining the two sets of displacement contours of moire fringes, i.e.  $u$ -fringes and  $v$ -fringes, and the linear strain-displacement relations (for small deformation), i.e.

$$\varepsilon_x = \frac{\partial u}{\partial x}, \quad \varepsilon_y = \frac{\partial v}{\partial y}, \quad \gamma_{xy} = \frac{\partial u}{\partial y} + \frac{\partial v}{\partial x} \quad (3.1)$$

the strain field of the loaded specimen can be found. In the above equations,  $u$  and  $v$  are displacement components in the  $x$ - and  $y$ -direction, respectively, while  $\varepsilon_x$ ,  $\varepsilon_y$  and  $\gamma_{xy}$  are the strain components of the surface under moire investigation.

The four laser beams required for the moire interferometry are generated from a moire interferometry system. The top view of the setup is shown in Figure 3.1. As can be seen, the point laser beam is diverged through a spatial filter and then redirected and collimated by a parabolic mirror. The enlarged collimated light is then illuminated onto four mirrors (designated as M in the diagram) located in the moire interferometer (outlined by a rectangle in the diagram because all components involved are attached to a fixture). The four mirrors, two horizontally positioned and two vertically positioned, form a cross pattern. (For clarity, only the two horizontal mirrors and beams are shown in the diagram.) The laser beams reflected from the four mirrors are redirected onto another four mirrors, which also form a cross pattern, for further beam angle adjustment. (Again, only the two horizontal mirrors and beams are shown in the diagram.) Details of the optical technique for moire interferometry can be found in a book authored by Post, Han and Ifju [3.12].

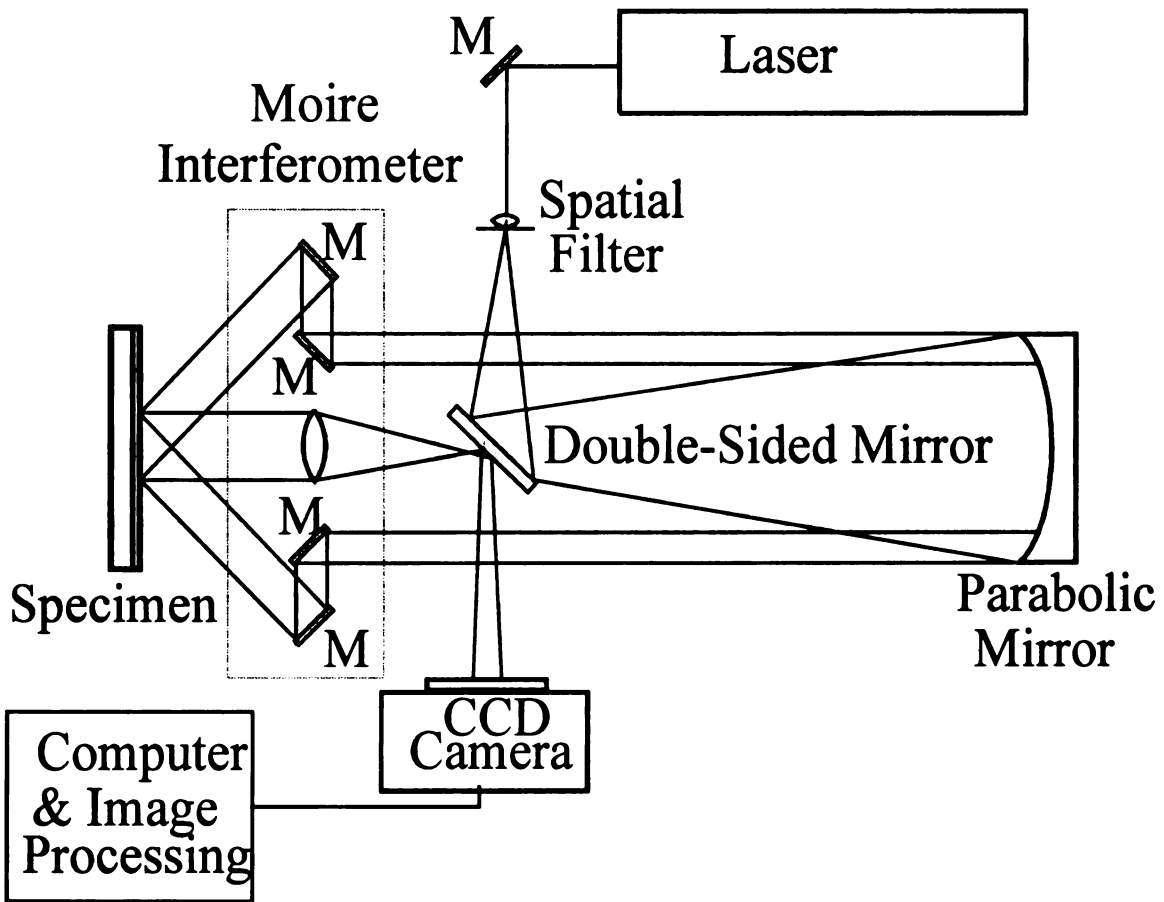


Figure 3.1 - Schematic diagram of optical setup for moiré interferometry (horizontal two beams only).

## **Experimental investigations**

### ***Moire on composite laminates***

Most studies on free-edge effect are based on analytical approaches. Very few studies are of experimental investigations. Pipes and Daniel [3.11] are the first to use a geometrical moire method to study the free-edge effect. The depth from free edges of composite laminates and influenced by the free edges is usually called the depth of boundary layer and has long been assumed to be approximately equal to the thickness of composite laminates. Mollenhaur [3.13] have identified the interlaminar shear strains around an open hole of a composite laminate subjected to uniaxial tension based on moire interferometry. The experimental results agree very well with analytical predictions.

Free edges of composite laminates have high interlaminar strains and high strain gradients due to the free-edge effect. Hence, they are critical locations in composite laminates. Since moire interferometry is an excellent method for surface measurements because of high sensitivity, it seems to be an ideal technique for studies of free-edge effect. However, moire interferometry has also been used for two-dimensional measurements based on plane strain or plane stress assumption. The validity of using strains obtained from moire interferometry for domains beyond free edges is an important issue for moire interferometry.



## ***Materials and testing***

In order to investigate the free-edge effect, both graphite/epoxy and glass/epoxy were used to prepare cross-ply laminates. The graphite/epoxy laminates were of 7-lamina plates and had a stacking sequence of  $[0/90/0/90/0/90/0]$ . Their thickness was 6mm. The glass/epoxy laminates, however, had three different stacking sequences, i.e.  $[0_7/90_7/0_7]$ ,  $[0_3/90_3/0_3/90_3/0_3/90_3/0_3]$  and  $[0/90/0/\dots]_{21}$ . These stacking sequences were designated as 3-lamina, 7-lamina and 21-lamina. The three types of glass/epoxy laminates were fabricated together and had identical thickness of 4.29mm.

All testing specimens were machined to have a length of 100mm but different widths. They were then subjected to four-point bending. The outer two loading points of the four-point bending fixture were located 75mm apart while the inner two loading points were 25mm apart. Both the outer loading points and the inner loading points were located symmetric with respect to the midspan of the composite laminates. Hence, there was an overhang of 12.5mm on each side of the specimens.

For moire interferometry, each specimen was coated with a moire grating along one edge. The moire grating included two sets of lines with constant spacing and parallel to the  $x$ - and  $y$ -axis, for measurements of displacement in  $y$ - and  $x$ -direction, respectively. Both sets of line had a frequency of 1200 lines/mm. The edge was then investigated by the moire interferometry system shown in Figure 3.1 when the specimen was under four-point bending.

## ***Effects of specimen width***

The free-edge effect, by name, was due to the existence of free edges in composite laminates. It actually covered the free edges of composite laminates and their vicinity. Hence, it was of a local phenomenon. The cause of free-edge effect was associated with mismatch of material properties due to sudden changes of fiber orientation or material through the laminate thickness. Since the depth of boundary layer was an important concern in laminate designs and a critical parameter for surface measuring techniques, composite laminates with various widths were investigated.

In this study, the aforementioned graphite/epoxy laminates were used for investigations of depth of boundary layer. Three widths, 25.4mm, 12.7mm and 6.35mm, were chosen. A 100mm-long laminate was first machined to have a width of 25.4mm. Once investigated by moire interferometry, the width was cut into half, i.e. 12.7mm, for a second moire investigation. It was again cut into half to have a width of 6.35 mm for a third moire investigation. During the second and the third cut on the specimen, the moire grating was protected from contamination by a thin-layer coating of silicon rubber.

The width of 25.4mm was about four times the laminate thickness. Because the boundary layer of a composite laminate was commonly assumed to be approximately equal to the thickness of the composite laminate [1], a composite laminate should have a minimum width twice the thickness to have a zone free from free-edge effect. Hence, 25.4mm was considered wide enough for

the graphite/epoxy laminate, which had a thickness of 6mm, to avoid interference of free-edge effects from both free edges. The 12.7mm specimen, however, had about the minimum width to avoid interference between the two free edges since it was about twice the laminate thickness. The 6.35mm specimen was expected to experience interference between the two free edges because it was only one-half of the minimum required width.

### ***Mismatch of material properties***

Since the free-edge effect was caused by mismatch of material properties through the laminate thickness, the significance of material type in the free-edge effect became an important issue. Hence, a glass/epoxy laminate also of 7-lamina stacking sequence, i.e.,  $[0_3/90_3/0_3/90_3/0_3/90_3/0_3]$ , was investigated to compare with the graphite/epoxy counterpart. In addition, the significance of different stacking sequences in the free-edge effect was also of interest. In the study, glass/epoxy laminates with stacking sequences of  $[0_7/90_7/0_7]$  and  $[0/90/0/\dots]_{21}$ , namely 3-lamina and 21-lamina, were also investigated to compare with the 7-lamina counterpart, i.e.  $[0_3/90_3/0_3/90_3/0_3/90_3/0_3]$ . In order to compare the three types of glass/epoxy laminate accurately, the composite specimens were fabricated together from a curing bag to warrant that an identical curing cycle was imposed and all laminates had similar thickness and fiber volume fraction.

## Results and discussions

### ***Strain Calculations***

The photographs of moire fringe patterns for displacement components in  $x$ -direction, i.e.  $u$ -fringes, and  $y$ -direction, i.e.  $v$ -fringes, for graphite/epoxy laminates with all three widths were shown in Figure 3.2. They were the images between the two inner loading points, i.e. within the constant moment zones. The magnification of the photographs could be obtained from comparing the height of the photographs with the thickness of graphite/epoxy laminates, i.e. 6mm. During the moire investigations, the photographs were taken by a CCD camera and recorded in a computer

For comparison, the force exerted on each loading point was set to be proportional to the specimen width. A force of 1112N was used for the 25.4mm specimen, 556N was used for the 12.7mm specimen and 278N for the 6.35mm specimen. By examining the photographs in Figure 3.2, the difference among the three cases was noticeable. However, it was also noted that the fringe patterns of all three cases were not of null field when there was no loading. Hence, a quantitative comparison of strain distributions was preferred over a qualitative description based on moire fringe patterns.

In order to recover the real strains, the initial fringes (at no loading) must be subtracted from the loaded counterparts. The procedures for finding the strain components  $\varepsilon_x$ ,  $\varepsilon_y$  and  $\gamma_{xy}$  could be based on the strain-displacement relations.

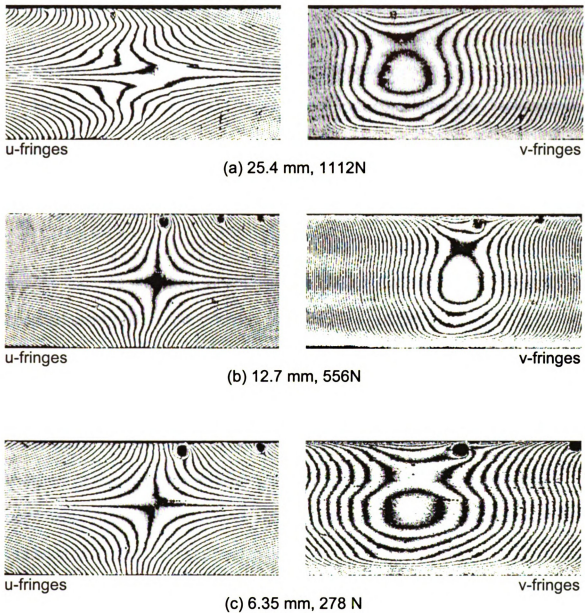


Figure 3.2 - Moiré fringe patterns for graphite/epoxy laminates with three different widths

A technique named vector analysis was also introduced briefly for finding shear strains. For demonstration purpose, only calculations of shear strains based on these two techniques were given below.

### **$\gamma_{xy}$ based on strain-displacement relations**

The shear strain  $\gamma_{xy}$  could be obtained from combining the displacement-fringe relations, i.e.

$$u = \frac{N_x}{f}, \quad v = \frac{N_y}{f} \quad (3.2)$$

and the linear strain-displacement relations given in Equation (3.1). Hence, it could be expressed by the following strain-fringe equation

$$\gamma_{xy} = \frac{1}{f} \left( \frac{\partial N_x}{\partial y} + \frac{\partial N_y}{\partial x} \right) \quad (3.3)$$

In the study, the frequency  $f$  of the moire interferometry system was 2400 lines/mm. It was twice the frequency of moire grating. Due to the nature four-point bending, the first component of Equation (3.3) was negligible. Accordingly, Equation (3.3) could be simplified to be

$$\gamma_{xy} = \frac{1}{f} \frac{\partial N_y}{\partial x} \quad (3.4)$$

The distribution of shear strain at a cross-section 6mm right to the midspan, i.e.  $x = 6\text{mm}$ , of the 25.4mm-wide graphite/epoxy composite laminate was of

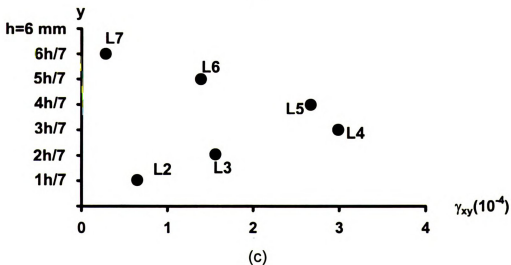
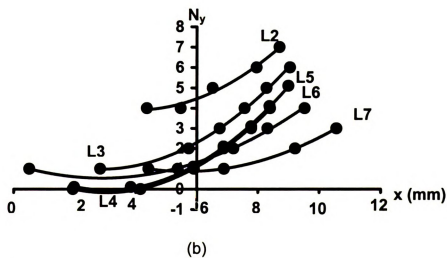
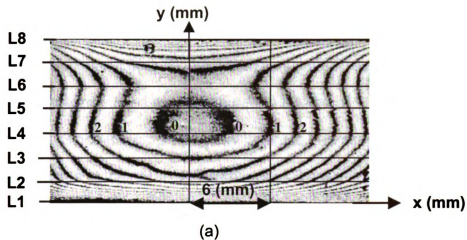


Figure 3.3 - Calculation of shear strain on the laminate interface based on least square method

interest. To begin with, the moire fringe orders, i.e.  $N_y$ , were assigned to the  $v$ -fringes as shown in Figure 3.3(a). Figure 3.3(a) was, in fact, exactly the same as Figure 3.2(a). The moire fringes were attributed to a force of 1112N exerted at each loading point. Since the graphite/epoxy laminate had seven laminae, the non-zero shear strains at the six laminate interfaces were of interest. These interfaces were designated as L2 to L7 in the diagram. Relations between the fringe order  $N_y$  and the  $x$ -coordinate for the six interfaces were then established and given in Figure 3.3(b) along with their least-squares curves. The shear strain at each interface was, in fact, the slope of each  $N_y$ - $x$  curve at  $x = 6\text{mm}$ . The six shear strains on the six laminate interfaces were shown in Figure 3.3(c) by solid circles. Apparently, the shear strain reached maximum around the midplane of the composite laminate.

The same procedures were used for laminates with widths of 12.7mm and 6.35mm. And similar procedures based on strain-displacement relations were also used for distributions of normal strains  $\varepsilon_x$  and  $\varepsilon_y$ .

### **$\gamma_{xy}$ Based on vector analysis**

Another technique to find  $\gamma_{xy}$  was called vector analysis. Shown in Figure 3.4(a) were the  $v$ -fringes identical to Figure 3.3(a). As a demonstration, the procedures to identify the shear strains at the intersecting point between the third laminate interface from the bottom of the composite laminate, i.e. the L4 line, and a vertical line located 6mm right to the midspan were performed.



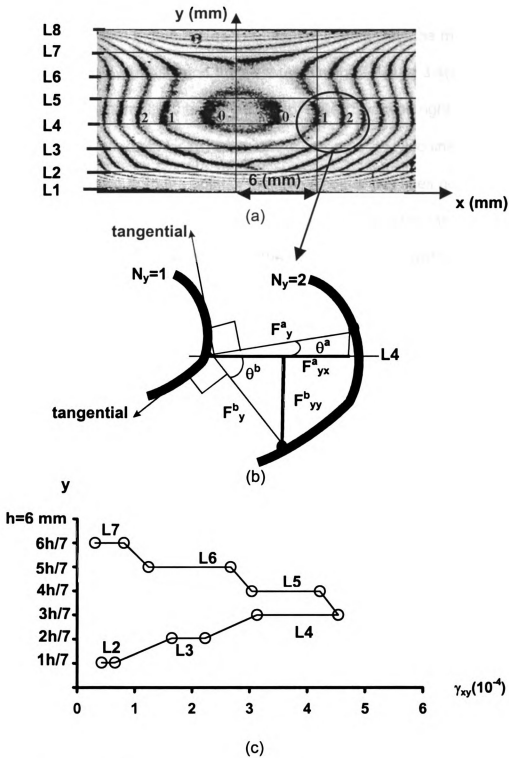


Figure 3.4 - Shear strain calculations based on vector analysis

To begin with, fringe orders were assigned to the fringes around the point of interest as shown in Figure 3.4(a). The point of interest and the moire fringes in the neighborhood were isolated from the remaining of Figure 3.4(a) and shown in Figure 3.4(b). Apparently, the moire fringe of order 1 passed right through the point of interest. Due to the kinky nature of the fringe  $N_y = 1$ , two lines tangent to the fringe were drawn from the point of interest. Another two lines normal to the two tangential lines were also drawn from the point of interest to the center of the neighboring fringe  $N_y = 2$ . The lengths of the two normal lines were designated as  $F_y^a$  and  $F_y^b$  as shown in Figure 3.4(b). The superscripts  $a$  and  $b$  represented for "above" and "below" the laminae interface, i.e. the L4 line, respectively, while the subscript  $y$  indicated that v-fringes were involved. The horizontal components of the two normal lines were named  $F_{yx}^a$  and  $F_{yx}^b$  while the vertical components were named  $F_{yy}^a$  and  $F_{yy}^b$ . For clarity, only  $F_{yx}^a$  and  $F_{yy}^b$  were shown in the diagram. The shear strain  $\gamma_{xy}$  for the lamina above the third interface and below the interface could be found as follows

$$\gamma_{xy}^a = \frac{F_{yx}^a}{f}, \quad \gamma_{xy}^b = \frac{F_{yx}^b}{f}. \quad (3.5)$$

If a point of interest did not coincide with a moire fringe, interpolation procedures should be imposed.

The shear strains on the laminate interfaces for the cross-section 6mm right to the midspan were shown in Figure 3.4(c). There were two shear strains on each laminate interface because shear strains were not continuous across the

laminated interface (though shear stresses were). It was noted that only one shear strain could be found for each laminated interface, if the technique based on the strain-displacement relations was used.

If a composite laminated had non-zero strains at no loading, the subtraction of initial strains from the loaded counterpart should be performed. Otherwise, the strains due to lower loading should be subtracted from those due to higher loading to recover the true strains.

### ***Depth of Boundary Layer***

Based on the techniques for strain calculations given above, the distributions of  $\epsilon_x$ ,  $\epsilon_y$  and  $\gamma_{xy}$  for the three widths of graphite/epoxy beams were found and shown in Figures 3.5, 3.6 and 3.7, respectively. Because initial fringes were not of null field in the graphite/epoxy laminates, subtractions of strains due to lower loading from higher loading were imposed. In the study, the fringes due to 890N, 445N and 222.5N for 25.4mm, 12.7mm and 6.35mm, respectively, were subtracted from those due to 1112N, 556N and 278N, respectively, resulting in net forces of 222N, 111N and 55.5N at each loading point, respectively. The distribution of  $\epsilon_x$  through the laminated thickness was given in Figure 3.5.

Apparently, there was hardly any difference among the three cases. A similar result was also found for the distribution of  $\epsilon_y$  through the laminated thickness, as shown in Figure 3.6.

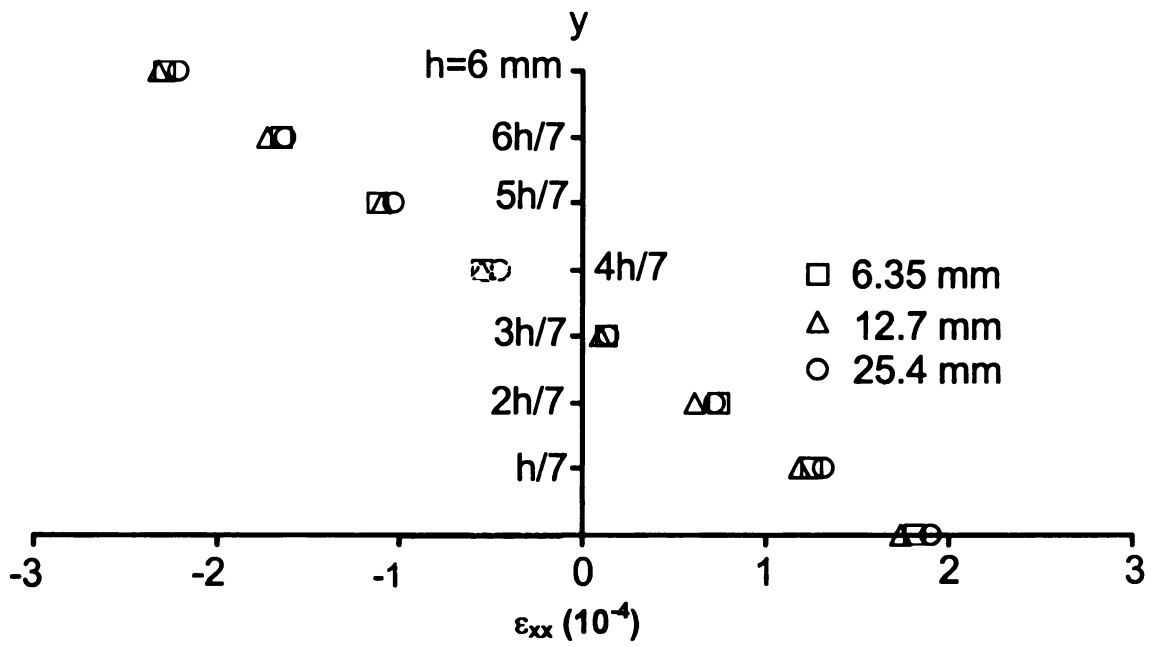


Figure 3.5 - Distribution of  $\epsilon_{xx}$  through laminate thickness

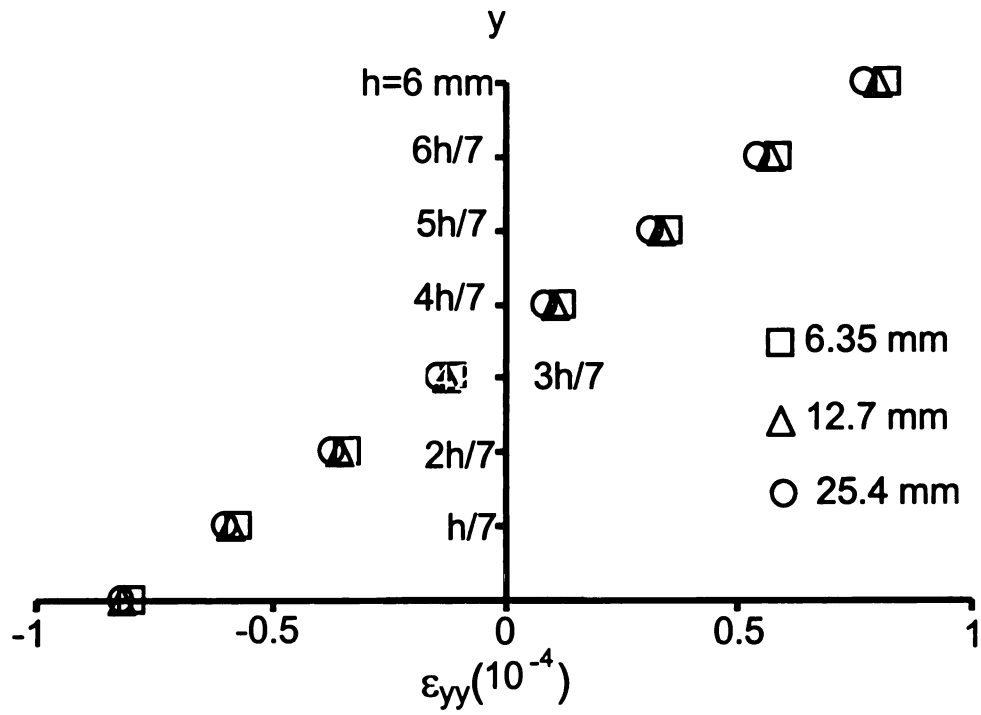


Figure 3.6 - Distribution of  $\epsilon_{yy}$  through thickness

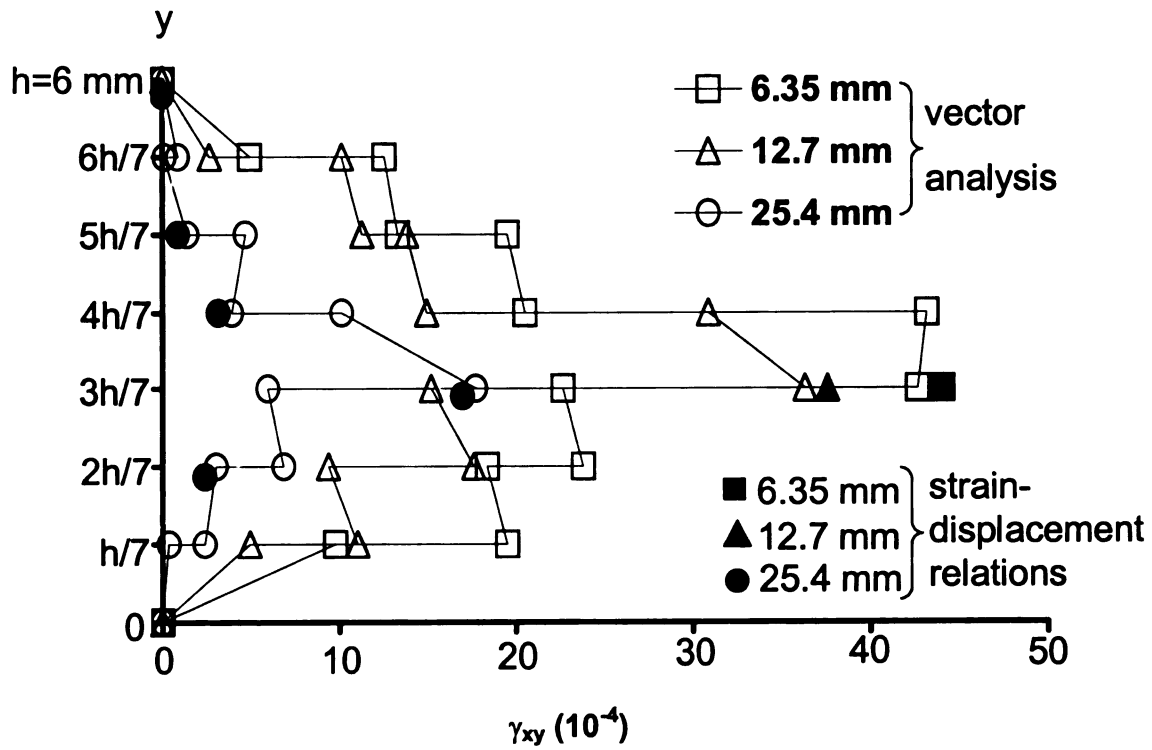


Figure 3.7 - The distribution of  $\gamma_{xy}$  through the laminate

The distribution of  $\gamma_{xy}$ , however, had a significant increase as the laminate width decreased as shown in Figure 3.7. This result was consistent with the fact that  $\gamma_{xy}$  was dependent on the free-edge effect. The maximum shear strain in the 12.7mm specimen showed a significant increase (actually more than doubled) from that in the 25.4mm one, implying that the boundary layer was greater than the laminate thickness as usually assumed. The maximum shear strain of the 6.35mm specimen was even higher than that of 12.7mm, indicating a much stronger effect from the free edges. The results from the strain-displacement relations agreed very well with those from the vector analysis.

### ***Effect of material type***

The moire fringes of glass/epoxy laminates with dimensions of 100mm by 25.4mm and thickness of 4.29mm were given in Figure 3.8. There were three types of stacking sequence, namely 3-lamina, 7-lamina and 21-lamina. All the  $u$ -fringes and  $v$ -fringes were due to a force of 111N at each loading point. However, the initial fringes at no loading were not of null field and must be subtracted from the loaded counterparts.

The distributions of  $\varepsilon_x$  and  $\varepsilon_y$  were about the same in all three cases as shown in Figures 3.9 and 3.10. These results were similar to those of graphite/epoxy case and again indicated that the normal strains were not subjected to the free-edge effect. However, the distributions of  $\gamma_{xy}$  in the three

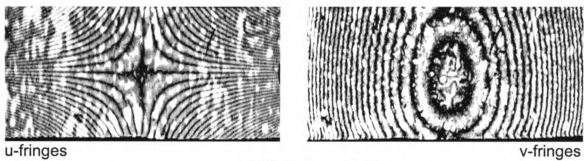
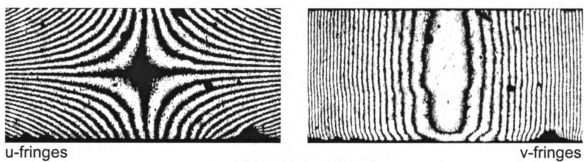
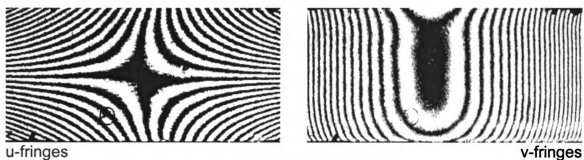


Figure 3.8 - Moire fringes of glass/epoxy laminates



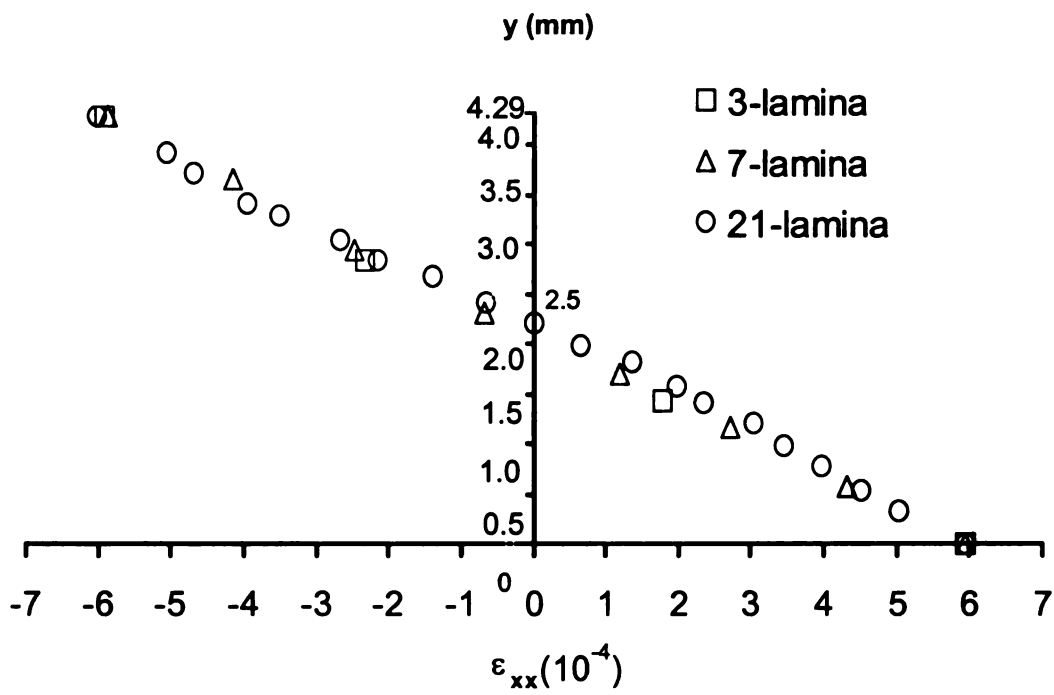


Figure 3.9 - Distribution of  $\epsilon_{xx}$  through laminate thickness

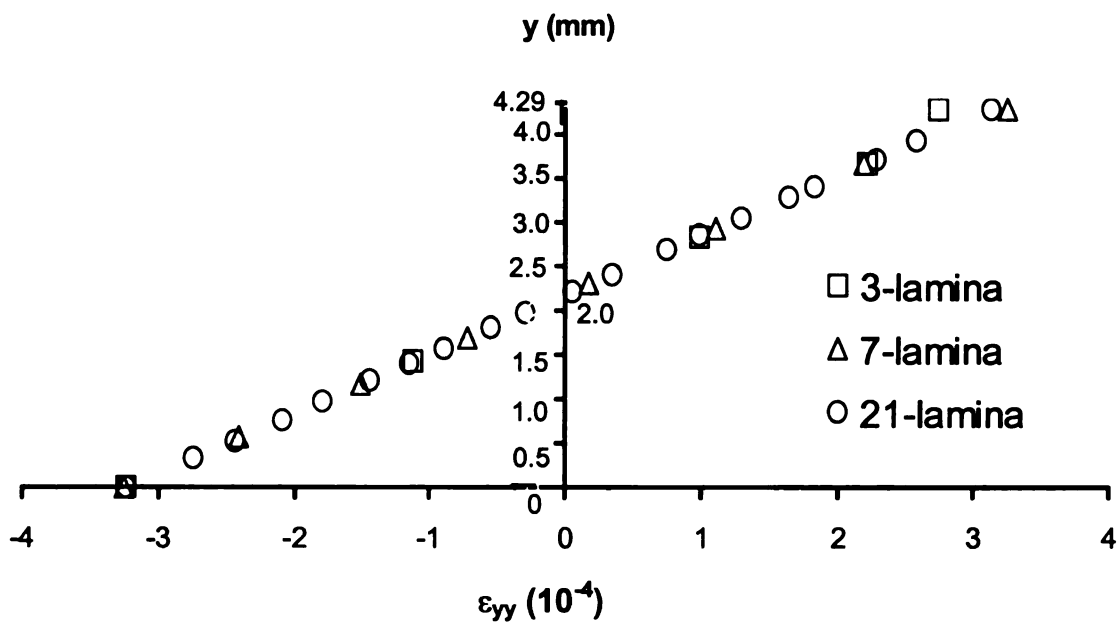


Figure 3.10 -Distribution of  $\epsilon_{yy}$  through thickness

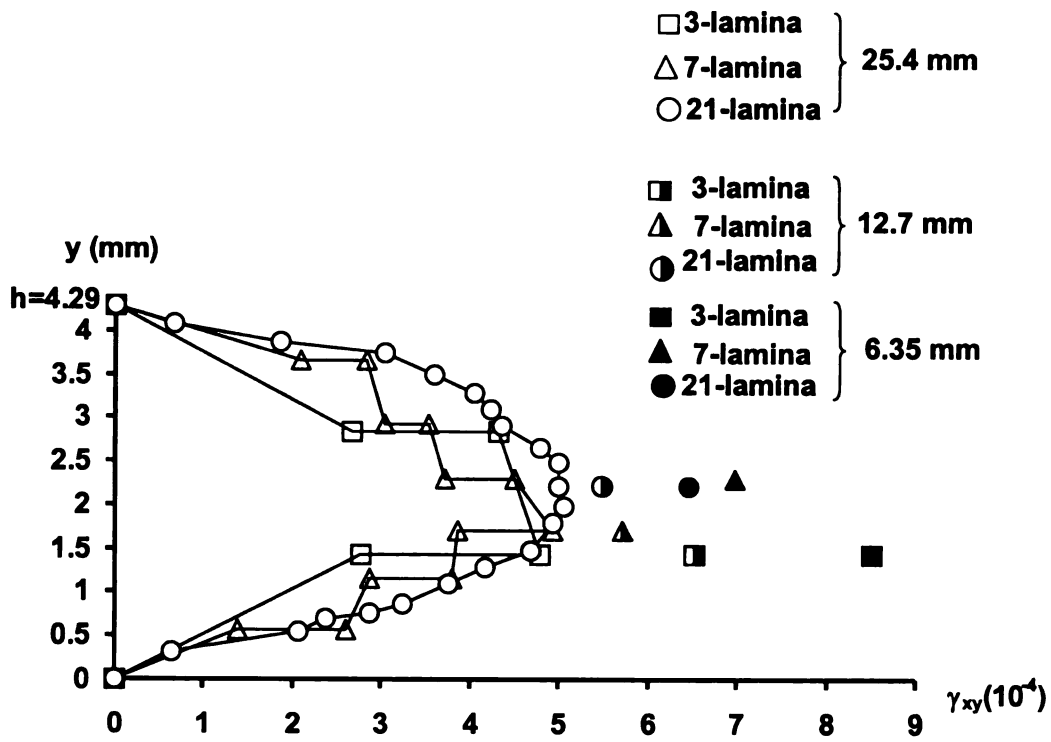


Figure 3.11 - Distribution of  $\gamma_{xy}$  through thickness

cases as shown in Figure 3.11 were different. Apparently, the higher the number of laminae, the smoother the distribution. However, the maximum shear strains of the three cases were very similar.

The difference of shear strains could also be found from comparing the 7-lamina glass/epoxy and the 7-lamina graphite/epoxy laminates. After considering the difference of thickness, the shear strain in the graphite/epoxy laminate was much higher than that in the glass/epoxy laminate. This result was believed to be attributed to the higher mismatch of material properties in graphite/epoxy than in glass/epoxy. In other words, graphite/epoxy had higher anisotropy than glass/epoxy; and the higher interlaminar strains due to the higher mismatch of material properties (between 0-lamina and 90-lamina) resulting from the higher anisotropy were responsible for the stronger free-edge effect.

### ***Effect lamination type***

According to Figure 3.11, the distribution of  $\gamma_{xy}$  in the 21-lamina specimen was much smoother than that in the 7-lamina one since the former had a much higher number of laminae through the thickness than the latter. In other words, the difference of shear strains across the laminate interfaces of the 21-lamina specimen was less than that in the 7-lamina one because the material mismatch between 0-lamina and 90-lamina was smaller than that between 0<sub>3</sub>-lamina and 90<sub>3</sub>-lamina. The 3-lamina specimen had the highest difference of shear strains among the three cases due to the highest material mismatch between 0<sub>7</sub>-lamina and 90<sub>7</sub>-lamina.

The distributions of  $\gamma_{xy}$  for the glass/epoxy beams with width of 12.7mm and 6.35mm were also given in Figure 3.11. They were obtained from loading the specimens with a force of 55.5N and 27.75N at each loading point, respectively. Surely, the initial strains at no loading should be subtracted from the loaded counterparts to reveal the true strains. Again, the changes of maximum shear strains due to the changes of width (from 25.4mm to 12.7mm and then to 6.35mm) were significant. However, the change in the 21-lamina was not as large as that in the 7-lamina, which was not as large as that in the 3-lamina.

## Conclusions

The moire interferometry is a surface technique for displacement measurements. Experimental results based on moire interferometry have revealed that the shear strains on free edges increase significantly as the width of a composite laminate decreases. However, the normal strains on free edges are not influenced by the free-edge effect. Accordingly, the normal strains based on moire interferometry could be used to represent the normal strains beyond the surface for plane-strain and plane stress problems. However, the shear strains based on moire interferometry should not be used beyond the surface at all because of the free-edge effect. Based on the results that shear strains change significantly with width changes, it has been found that the depth of boundary layer is greater than the thickness of composite laminates as usually assumed.

The free-edge effect is associated with mismatch of material properties. Since graphite/epoxy has higher anisotropy than glass/epoxy, a composite

laminates made of graphite/epoxy experience a stronger free-edge effect than the glass/epoxy counterpart. Similarly, a composite laminate consisting of thicker laminae has a higher mismatch of material properties among laminae and hence is more strongly influenced by free edges than that consisting of thinner laminae.

## **Acknowledgements**

The author wishes to express his sincere thanks to Professor Daniel Post of Virginia Tech for providing the blue prints of building the moiré interferometry system used in the study and many valuable discussions on moiré interferometry. Thanks also extended to Professor Peter Ifju of University of Florida for providing the original moiré grating and many valuable discussions on grating preparations. The financial support from Michigan Research Fund is also greatly appreciated.

## References

- 3.1 Pipes, R, Pagano, N. "Interlaminar Stresses in Composite Laminates Under Uniform Axial Extension," *Journal of Composite Materials*, Vol. 4, 538-548, (October 1970).
- 3.2 Becker, W., " Closed-form Solution for the free-edge effect in cross-ply laminates," *Composite Structures*, Vol. 26, 39-45, (1993).
- 3.3 Lessard, L., Schmidt, A, and Shokrieh, M, "Three-Dimensional Stress Analysis of Free-Edge Effects in Simple Composite Cross-Ply Laminate," *International Journal of Solid Structures*, Vol. 33, No. 15, 2243-2259, (1996).
- 3.4 Becker, W., Jin, P., Neuser, P., " Interlaminar Stresses at the Free Corners of a Laminate," *Compostie Structures*, Vol. 45, 155-162, (1999).
- 3.5 Altus, E, Rotem, A, Shmueli, M, "Free Edge Effect in Angle Ply Laminates- A new Three Dimensional Finite Diffrencece Solution," *Journal of Composite Materials*, Vol. 14, 21-30, (January, 1980).
- 3.6 Wang, A, Crossman, F., " Some New Results of Edge-Effect in Symmetric Composite Laminates," *Journal of Composite Materials*, Vol. 11, 92-106, (January, 1977).
- 3.7 Chaudhuri, R, Xie, M, "Free-Edge Stress Singularity in a Bimaterial Laminate," *Composite Structures*, Vol. 2, 129-136, (1998).
- 3.8 Becker, W., " Closed-form solution for the Free-Edge Effect in Cross-Ply Laminates," *Composite Structures*, Vol 26, 39-45, (1993).
- 3.9 Zhang, C., and Yeh, H., "A Variation Approach for Straight Edge Stresses in Laminated Composites," *Composite structures*, Vol. 43, 243-254, (1998).
- 3.10 Oplinger, W., Parker B., and Chiang, F., "Edge-Effect Studies in Fiber-reinforced Laminates," *Experimental Mechanics*, 347-354, (September 1974).
- 3.11 Pipes, B., and Daniel, I, " Moire Analysis of the interlaminar Shear Edge-Effect in Laminated Composites," *Journal of Composite Materials*, Vol. 5, 255-259, (April 1971).
- 3.12 Post, D., Han, B., and Ifju, P., *High Sensitivity Moire*, Springer-Verlag,

1993.

- 3.13 Mollenhauer, D. " Interlaminar Deformation at Hole in Laminated Composites: A detailed Experimental Investigation Using Moire Interferometry," Ph.D. Dissertation, Virginia Polytechnic Institute and State University, Blacksburg, VA, August 1997.
- 3.14 Herakovich, C., Post, D., Buczek, M., and Czarnek, R., "Free-Edge Strain Concentrations in Real Composite Laminates: Experimental-Theoretical Correlation," Journal of Applied Mechanics, Vol. 52, 787-793, (December 1985).
- 3.15 Post, D., "Moire Interferometry; Advances and Applications," Experimental Mechanics, 276-280, (September 1991)



## Chapter 4

### JOINING FORCES IN ASSEMBLED COMPOSITE BEAMS

#### **Abstract**

This study investigated the joining force of assembled composite beams. Two identical composite laminates made of cross-ply glass/epoxy were joined via various joining techniques such as adhesive bonding, mechanical riveting, stitching joining and combinations of these techniques. The assembled two-laminate composite beams were loaded by four-point bending. The corresponding normal strains were identified by moire interferometry. Depending on the joining condition between the laminates, the moire patterns of u-fringes and v-fringes may be continuous or discontinuous across the joining interface. To quantify the joining condition, two analytical models based on the Classical Beam Theory, the interface model and the interphase model, were presented. The joining forces of the assembled composite beams were identified. Mechanical riveting was found to be an efficient joining technique for assembling the thin composite laminates.

## Introduction

Due to their high stiffness-to-weight and high strength-to-weight ratios, fiber-reinforced polymer matrix composite materials have found many applications in high-performance structures. These composite materials are usually used in thin-laminate form. As the technologies of composite materials advance, more and more thick-section composite laminates are manufactured [4.1] and used in various industries. However, the manufacturing cost for thick composite laminates could become unaffordable. This is especially true when uniform properties through the laminate thickness are of primary concern.

In an effort to reduce the manufacturing cost and to avoid non-uniform properties through the laminate thickness, *assembled* composite plates have been considered as alternatives to thick *laminated* composite plates [4.2].

Assembled composite plates are constructed by assembling multiple thin composite laminates together via various joining techniques. In a previous study [4.2], techniques including mechanical riveting, adhesive bonding, stitching joining [4.3,4.4], and their combinations have been used in assembling thin composite laminates. Those experimental results revealed that joining stiffness plays an important role in impact resistance. The results suggest that a better joint gives higher joining stiffness and subsequently higher perforation threshold.

As an effort to investigate the joining conditions of assembled composite laminates based on various joining techniques and to quantify the joining conditions, both analytical modeling and experimental investigation are presented in this study.

## **Analytical modeling**

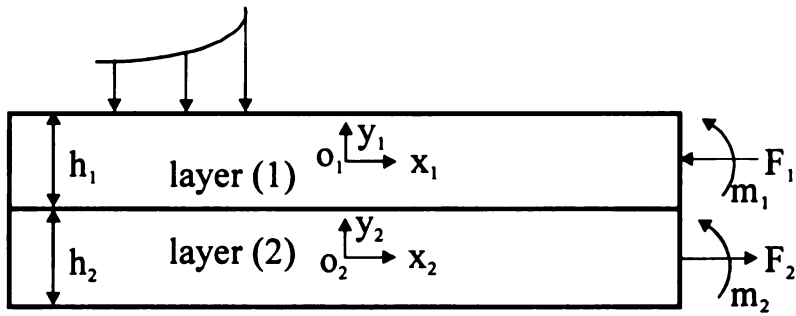
In order to quantify the joining conditions of assembled composite beams based on various joining techniques, two analytical models were presented. They were *the interface model* and *the interphase model*. Although these models could be applied to assembled composite beams consisting of multiple laminates, only those beams made up of two laminates were of interest in the study. The interface model assumed that the joining interface between the two composite laminates had no thickness. However, the interphase model considered that there was a finite thickness, i.e. an interphase layer, between the laminates. All the assembled composite beams investigated in the study had an effective length of 75 mm (between the two outer rollers of the four-point bend fixture) and a nominal thickness about 6.4 mm, resulting in an aspect ratio of length-to-thickness around 11.7. Accordingly, both the interface and interphase models were developed based on the Classical Beam Theory.

### ***The interface model***

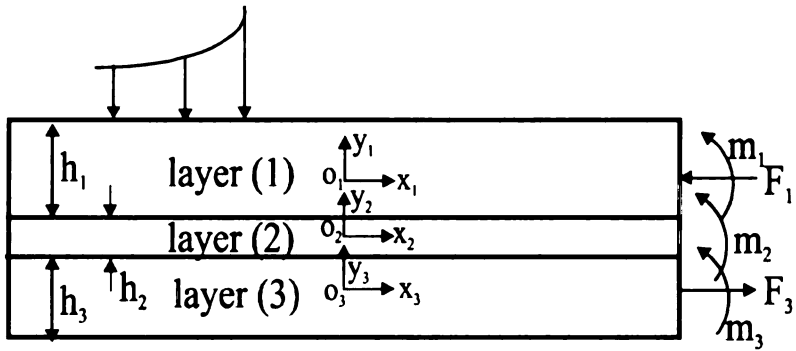
This model considers that assembled composite beams consist of two layers and a joining interface. Each layer could be made up of a composite

laminates and the joining interface between the layers is assumed to have no thickness. Accordingly, the finite dimensions of the bonding interfaces due to adhesive and double-coated tape in real joining practice are neglected. As shown in Figure 4.1(a), the free-body diagram of an interface model is subjected to transverse loading because the transverse loading can help to characterize the joining condition of the assembled composite beam. In addition, two resultant forces  $F_1$  and  $F_2$  and two resultant bending moments  $m_1$  and  $m_2$  are also added to Figure 4.1(a). It should be noted that these resultant forces and moments are of internal force components and, for convenience, they are shown on the generic cross-sections along the longitudinal axes ( $x_1$  and  $x_2$ ) of the composite layers. The internal force components should not be mixed up with the external forces, such as the transverse loading, usually depicted on the surfaces of a free-body diagram.

When the two composite layers are not assembled by any joining technique, each layer is expected to behave independently if there is no friction between them. The resultant forces  $F_1$  and  $F_2$  should vanish because there is no force transferring between the two layers. The primary stress, i.e. the normal stress along the  $x$ -direction, in each layer can then be calculated directly from the flexure formula. However, if the two layers are assembled together by any joining technique, there will be load transferring between them, and  $F_1$  and  $F_2$  will no longer be zero. The resultant bending moments  $m_1$  and  $m_2$ , however, are not directly tied to the joining condition. They are more related to the external force, i.e. the transverse loading.



(a)



(b)

Figure 4.1 - Free body diagrams for: (a) the interface model, and (b) the interphase model

The geometry and the coordinate systems of the interface model are shown in Figure 4.1(a). According to the diagram,  $x_i o_i y_i$  is the local coordinate system of layer ( $i$ ) that has a thickness of  $h_i$ . If layer (1) and layer (2) are made of the same material and have identical dimensions, the following equations should hold:

$$h_1 = h_2, \quad A_1 = A_2, \quad E_1 = E_2, \quad I_1 = I_2, \quad (4.1)$$

where  $A_i$  is the cross-sectional area,  $E_i$  is the Young's modulus and  $I_i$  is the second moment of area of layer ( $i$ ). Based on strength-of-materials analysis, the normal stresses along the longitudinal axes ( $x_1$  and  $x_2$ ) of the composite layers can be expressed by the following equations:

$$\begin{aligned} \sigma_x^{(1)} &= -\frac{F_1}{A_1} - \frac{m_1}{I_1} y_1 \\ \sigma_x^{(2)} &= \frac{F_2}{A_2} - \frac{m_2}{I_2} y_2 \end{aligned} \quad (4.2)$$

According to equilibrium of forces, the two resultant forces have opposite sense but identical magnitude, i.e.

$$F_1 = F_2. \quad (4.3)$$

When the two layers are joined together by any means, both the individual layers and the assembled beam have an identical bending curvature  $\kappa$ , i.e.

$$\kappa = \frac{m_1}{E_1 I_1} = \frac{m_2}{E_2 I_2} = \frac{m_1 + m_2}{E_1 I_1 + E_2 I_2} \quad (4.4)$$

Since  $E_1 I_1 = E_2 I_2$  (from Equation (4.1)), it yields

$$m_1 = m_2. \quad (4.5)$$

From equilibrium of moments, the sum of the two resultant bending moments and the moment generated by the two resultant forces should be equal to the bending moment due to the transverse loading. By defining

$$M = m_1 + m_2 + \frac{F_1 (h_1 + h_2)}{2} \quad (4.6)$$

as the total bending moment due to the transverse loading for the generic cross-section of the composite beam, the normal stresses given in Equation (4.2) can be rewritten as

$$\sigma_x^{(1)} = -\frac{F_1}{A_1} + \frac{F_1 h_1}{2I_1} y_1 - \frac{M}{2I_1} y_1 \quad (4.7)$$

$$\sigma_x^{(2)} = \frac{F_1}{A_1} + \frac{F_1 h_1}{2I_1} y_2 - \frac{M}{2I_1} y_2$$

When there is no joining between the two layers, the resultant force  $F_i$  should vanish because the two layers are not related to each other and there is no load transferring between them. Equation (4.7) can then be simplified to be

$$\sigma_x^{(1)} = \sigma_x^{(2)} = -\frac{M}{2I_1} y_1. \text{ These results imply that the normal stresses in the two}$$

composite layers are equal to each other and each is attributed to 50% of the

total bending moment  $M$  (i.e.  $m_1 = m_2 = M/2$ ) due to the transverse loading. However, as the joining condition improves, the load transferring between the layers also increases, and a finite resultant force will exist. Hence, the resultant force is actually the joining force between the two layers and can be used to quantify the joining condition of assembled composite beams.

### ***The interphase model***

This model considers that assembled composite beams consist of three layers as shown in Figure 4.1(b). The two outer layers are of composite laminates; whereas the interphase layer is a joining layer, which could be either fictitious or real. The assumption of an interphase layer seems to be real for composite beams assembled by adhesive or double-coated tape, which have a uniform thickness between the composite layers. However, the assumption of an interphase layer is only fictitious for joints that are based on mechanical riveting and stitching.

The geometry and coordinate systems for the interphase model subjected to transverse loading are shown in Figure 4.1(b) along with the resultant force  $F_i$  and the bending moment  $m_i$  at the generic cross-sections along the longitudinal axes of the layers. In the cases where layer (1) and layer (3) are identical in both material and dimensions, the following equations hold:

$$h_1 = h_3, \quad A_1 = A_3, \quad E_1 = E_3, \quad I_1 = I_3. \quad (4.8)$$



And the normal stresses in the three layers can be expressed by the following equations:

$$\sigma_x^{(1)} = -\frac{F_1}{A_1} - \frac{m_1}{I_1} y_1$$

$$\sigma_x^{(2)} = -\frac{m_2}{I_2} y_2 \quad (4.9)$$

$$\sigma_x^{(3)} = \frac{F_3}{A_3} - \frac{m_3}{I_3} y_3$$

Based on equilibrium of forces, the two resultant forces have opposite sense but the same magnitude, i.e.

$$F_1 = F_3. \quad (4.10)$$

Because all three layers are assembled together, they have an identical bending curvature  $\kappa$ , i.e.

$$\kappa = \frac{m_1}{E_1 I_1} = \frac{m_2}{E_2 I_2} = \frac{m_3}{E_3 I_3} = \frac{m_1 + m_2 + m_3}{E_1 I_1 + E_2 I_2 + E_3 I_3} \quad (4.11)$$

Since  $E_1 I_1 = E_3 I_3$  (based on Equation (8)), it yields

$$m_1 = m_3. \quad (4.12)$$

By defining

$$M = m_1 + m_2 + m_3 + F_1(h_1 + h_2) \quad (4.13)$$

as the total bending moment due to the transverse loading for the generic cross sections shown in Figure 4.1(b), the normal stresses given in Equation (4.9) can be rewritten as

$$\begin{aligned}\sigma_x^{(1)} &= -\frac{F_1}{A_1} + \frac{F_1(h_1 + h_2)E_1}{2E_1I_1 + E_2I_2} y_1 - \frac{ME_1}{2E_1I_1 + E_2I_2} y_1 \\ \sigma_x^{(2)} &= \frac{F_1(h_1 + h_2)E_2}{2E_1I_1 + E_2I_2} y_2 - \frac{ME_2}{2E_1I_1 + E_2I_2} y_2 \\ \sigma_x^{(3)} &= \frac{F_1}{A_1} + \frac{F_1(h_1 + h_2)E_1}{2E_1I_1 + E_2I_2} y_3 - \frac{ME_1}{2E_1I_1 + E_2I_2} y_3\end{aligned}\tag{4.14}$$

According to Equation (4.14), the resultant force  $F_i$  and the bending rigidity of the interphase layer  $E_2I_2$  (or even the Young's modulus of the interphase layer  $E_2$ ) can be identified, if the following are known: the normal stresses, the dimensions and the Young's modulus of the composite layers. As mentioned earlier, the resultant force is related to the load transferring between the composite layers. Therefore, the resultant force is really the joining forces of the assembled composite beam. Similarly, since the bending rigidity is associated with the property of the joining layer, that bending rigidity can represent the joining condition of the assembled composite beam. However, if the bending rigidity of the interphase layer  $E_2I_2$  can be neglected (either because the interphase layer is too thin or the modulus is too low), the first and the third equations of Equations (4.14) can be simplified as

$$\sigma_x^{(1)} = -\frac{F_1}{A_1} + \frac{F_1(h_1 + h_2)}{2I_1} y_1 - \frac{M}{2I_1} y_1 \quad (4.15)$$

$$\sigma_x^{(3)} = \frac{F_1}{A_1} + \frac{F_1(h_1 + h_2)}{2I_1} y_3 - \frac{M}{2I_1} y_3$$

These two equations are identical to those presented in the interfacial model, i.e. Equation (4.7). The second equation of Equation (4.14), however, becomes trivial.

## Experimental investigations

### *Composite laminates*

In experimental investigations, assembled composite beams were made up of glass/epoxy laminates which had a stacking sequence of  $[0/90/0/\dots]_{13}$  and a nominal thickness of 3.2 mm. The dimensions of the composite laminates used as building blocks for the assembled composite beams were 100 mm x 25 mm. Every two composite laminates were joined to form a two-laminate beam. The assembled composite beams were then subjected to four-point bending.

As shown in Figure 4.2(a), the distance between the inner rollers of the bending fixture was 25 mm while that between the outer rollers was 75 mm. Accordingly, the assembled composite beams had an effective length of 75 mm (the distance between the outer rollers) and a total thickness around 6.4 mm (twice the laminate thickness although the true thickness of an assembled composite beam was also dependent on the thickness of the joining layer). In

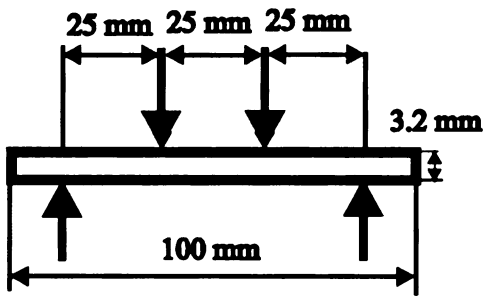
addition, it should be noted that the bending moment  $M$  between the inner rollers was constant and equal to  $25P$  Nmm (where  $P$  was the force exerted on the composite beam by each roller) and the shearing force within the interval vanished.

### ***Joining techniques***

Many joining techniques such as mechanical riveting, adhesive bonding, stitching joining, and their combinations were performed in the study. Figures 4.2(a)–4.2(f) showed schematic diagrams (either side view or top view) of some assembled composite beams used in the study. Details of the designations for all the assembled beams investigated in the study were given below.

- A. ONE (for one-laminate beam) – Shown in Figure 4.2(a) was the side view of a single composite laminate used as the building block for assembled composite beams. The single laminate had a nominal thickness of 3.2 mm. Details of the four-point bending configuration was also shown in the diagram.
- B. 2B (2 for two-laminate beam and B for bonding) – As shown in Figure 4.2(b), two composite laminates were bonded together by a room-temperature curing epoxy. The thickness of the bonding layer was around 0.2 mm. Thus, the total thickness of the assembled composite beam was around 6.6 mm.
- C. TWO (for two laminates) – Two composite laminates were simply piled up together without any form of joining between them. However, a small amount of epoxy used as moire grating applied to one edge of the assembly was found to infiltrate the interface between the laminates and might effectively join the laminates up to some extent.

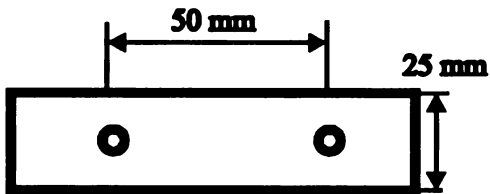
- D. 2T (2 for two-laminate and T for taping) – Two composite laminates were joined together by a double-coated tape. The tape was about 0.1 mm thick.
- E. 2R2 (the first 2 for two-laminate, R for riveting and the second 2 for two rivets per 50 mm) – Two composite laminates were joined together through the



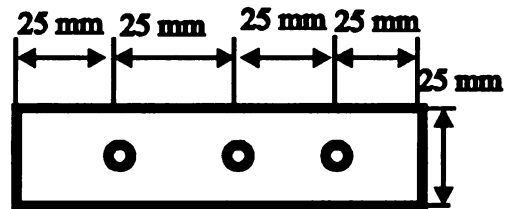
(a) ONE



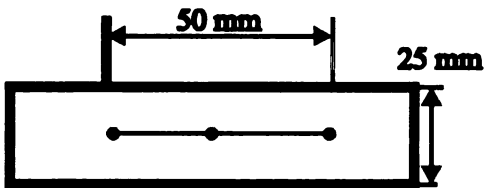
(b) 2B



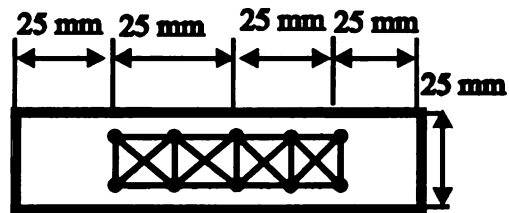
(c) 2R2



(d) 2R3



(e) 2S3



(f) 2S5

Figure 4.2 - Schematic diagram of various joining techniques

laminates by two rivets. Figure 4.2(c) showed the top view of the assembly. During riveting, two holes were prepared by a #30 drilling bit before 4x580 steel rivets (1/8" in diameter and 1/4" in grip) were pushed in by a riveting hand gun. The two rivets were located along the centerline of the beam and the distance between them was 50 mm. They were also symmetric with respect to the mid-span of the assembled beam.

- F. 2R3 (R for riveting and 3 for three rivets per 50 mm) – Instead of two rivets used in 2R2, three rivets evenly separated within the same 50 mm interval were employed. Figure 4.2(d) showed the top view of the joining configuration.
- G. 2R4 (R for riveting and 4 for four rivets per 50 mm) – Similar to the 2R2 and 2R3 cases, two composite laminates were joined together. However, four rivets were employed in the 50-mm interval. As a result, the inner rollers of the bending fixture were located right on top of two inner rivets.
- H. 2BR3 (B for bonding, R for riveting and 3 for three rivets per 50 mm) – Two composite laminates were first bonded by the epoxy used in the 2B case. They were then further joined together by three rivets with a pattern identical to the 2R3 case.
- I. 2S3 (S for stitching and 3 for three stitches per 50 mm) – Two composite laminates were joined together by hand stitches through the laminate thickness as shown in Figure 4.2(e). Before performing the stitches, three holes with locations identical to those in the 2R3 case were prepared. The

holes were formed by a drilling bit of 1/16" in diameter. A steel wire of 28 gauge was used as the stitching line.

- J. 2S5 – (S for stitching and 5 for 5-by-2 stitching pattern) Two composite laminates were joined together with a 5-by-2 stitching pattern (totally ten stitching holes) within a 50mm-by-12.5mm area as depicted in Figure 4.2(f). For each four nodes forming a square unit, there were totally six stitching lines, i.e. two horizontal, two vertical and two diagonal lines, on each side of the assembly.
- K. 2BS3 (B for bonding, S for stitching and 3 for three stitches per 50 mm) – Two composite laminates were first bonded by the epoxy used in the 2B case and then stitched together by the stitching pattern used for 2S3.

### ***Moire interferometry***

The interface and the interphase models presented earlier were based on two-dimensional analysis. Examining Equation (4.7) of the interface model and Equation (4.14) of the interphase model revealed that the information regarding the normal stress  $\sigma_x$  through the laminate thickness  $y_i$  was required for identifying the resultant force  $F_i$  (for both models) and the bending rigidity  $E_2I_2$  of the interphase layer (for the interphase model only). The resultant force and the bending rigidity, in fact, represented the joining force and the joining condition, respectively, of the assembled composite beams.

Accordingly, an experimental technique that could provide the needed stress information through the laminate thickness would be useful in finding the



joining force and the joining condition. Due to its high sensitivity and high accuracy, moire interferometry was chosen for the stress analysis.

Moire interferometry is a displacement-based technique. To perform moire interferometry, assembled composite beams must be coated with a layer of moire grating on one edge. Details of the one-layer grating technique used in the study are found in Reference [4.5]. The grating-coated assembled beams were then loaded by four-point bending. The deformation of each beam could then be investigated by a moire interferometer.

The top view of the moire interferometry setup used in the study was shown in Figure 4.3. However, details of the optical technique are found in a book authored by Post, Han and Ifju [4.6]. As shown in Figure 4.3, the point laser beam was diverged through a spatial filter and then redirected and collimated by a parabolic mirror. The enlarged collimated light was then illuminated onto four mirrors (designated as M in the diagram) located in the moire interferometer. The four mirrors, two horizontally positioned and two vertically positioned, formed a cross pattern. For clarity, only the two horizontal mirrors and beams were shown in the diagram. The laser beams reflected from the four mirrors were redirected onto another four mirrors (also formed a cross pattern) for further beam angle adjustment. Again, only the two horizontal mirrors and beams were shown in the diagram.

Moire interferometry is based on optical diffraction and interference. As the two horizontal beams reflected from the second set of mirrors, the beams

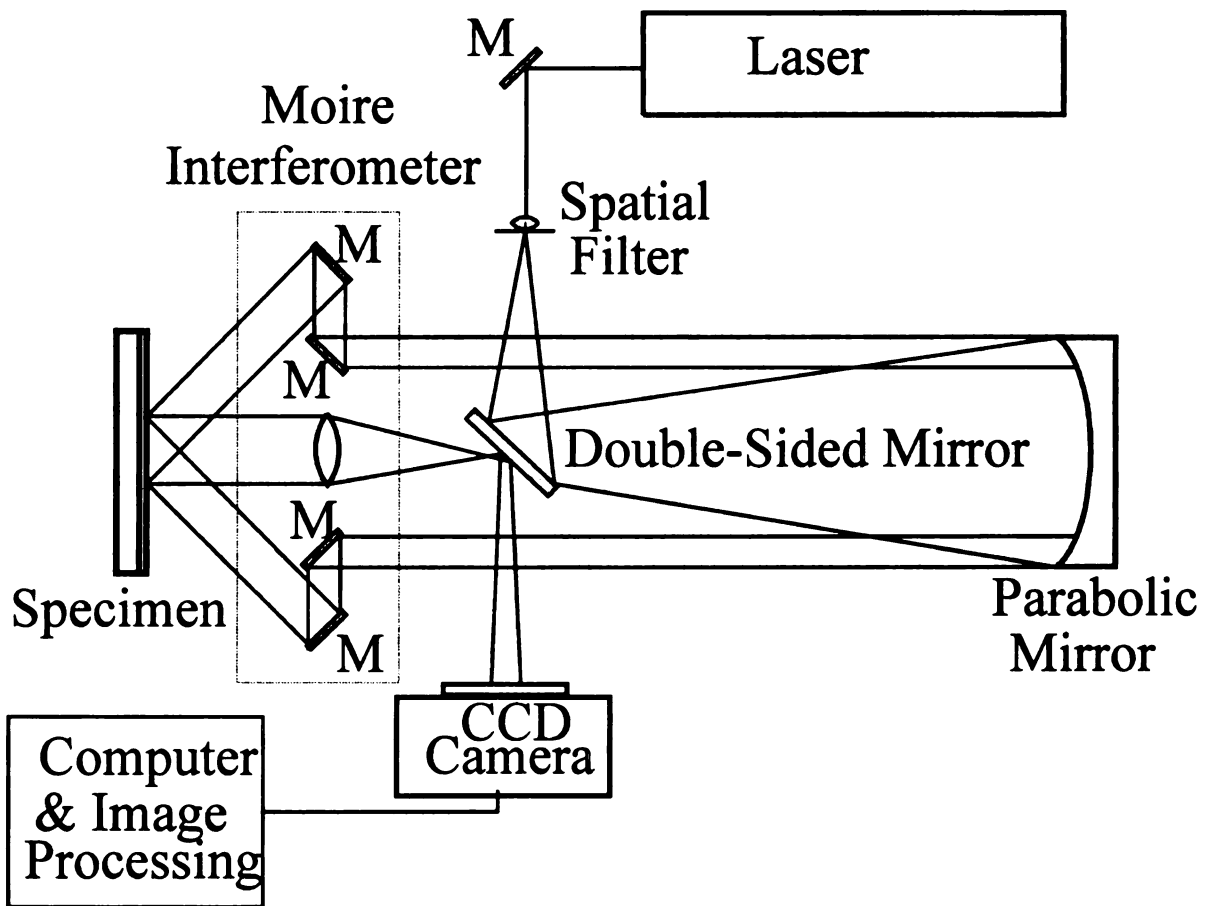


Figure 4.3 - Schematic diagram of optical setup for moiré interferometry (horizontal two beams only)

were illuminated onto the specimen surface (actually edge) that was coated with a layer of moire grating. Due to the high frequency (1200 lines/mm) of the moire grating used in the study and its mirror-like surface, the two horizontal beams were then diffracted reflectively by the grating. Under no-loading condition, two (one from each horizontal beam) diffracted beams of the first-order should emit from the specimen edge. If the angles of the second set of mirrors were adjusted properly according to the grating frequency, the two diffracted beams should be both normal to the specimen surface and cause no interference between them. However, if the specimen is deformed due to transverse loading, the frequency and orientation of the moire grating lines on the specimen edge would be altered. In this state the diffracted beams would be neither parallel to each other nor normal to the specimen edge any more. As a result, interference between them would take place and a moire fringe pattern representing the contours of constant displacement would be formed right on the specimen edge.

The two horizontal beams could provide contour lines for displacement along the longitudinal direction ( $x$ -direction), namely  $u$ -fringes, whereas the two vertical beams (not shown in the diagram) could give contour lines for displacement through the thickness direction ( $y$ -direction), namely  $v$ -fringes. The strain field of the deformed composite beam could then be calculated from the displacement contour lines, i.e. moire fringe patterns, with the use of linear strain-displacement relations. Because the assembled composite beams had an aspect ratio of 11.7 and they were subjected to small transverse loading in the study, the

normal stress  $\sigma_x$  was the primary component in the stress analysis. Accordingly, only u-fringes were required for stress analysis.

## **Results and conclusions**

### ***Moire fringe patterns***

The assembled composite beams were loaded by four-point bending. Moire patterns of u-fringes and v-fringes at several loading levels were recorded by a CCD camera and stored in a computer for later analysis. The u-fringes played a primary role on joining analysis for the purpose of calculation. Figures 4.4(b) – 4.4(l) displayed both u-fringes and v-fringes for the two-laminate beams due to a force of 45 N at each loading point (roller), i.e.  $P = 45$  N. This loading level resulted in a constant bending moment of 1125 Nmm between the two inner rollers. Hence, only the moire patterns within the pure bending zone were presented. For comparison, the moire fringes of the ONE case based on  $P = 22.5$  N were also given in Figure 4.4(a). Note also that the fringe patterns at no-loading condition were not of null field due possibly to misalignment of the optical system and shrinkage of moire grating during replication process.

- A. ONE – The moire patterns of u-fringes and v-fringes were shown in Figure 4.4(a). Both were symmetric with respect to the longitudinal and thickness axes. It was believed that an assembled two-laminate composite beam with perfect joining should have fringe patterns identical to the patterns in Figure 4.4(a).

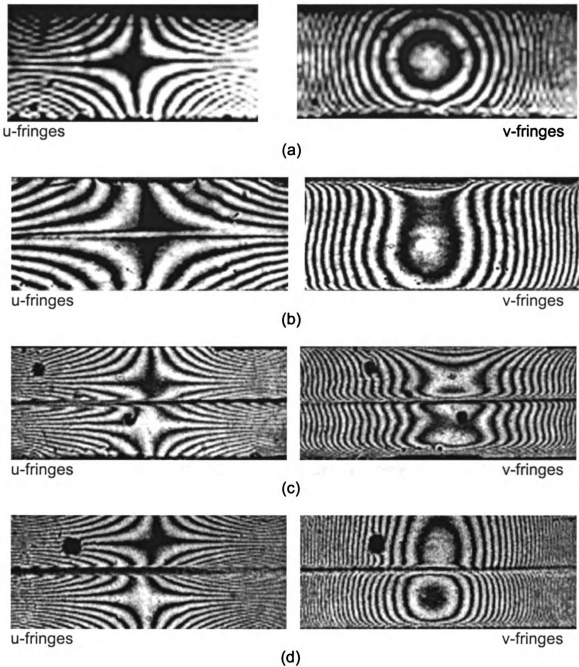


Figure 4.4 - Moire fringe pattern for: (a) ONE (one laminate beam), (b) 2B (2 for two-laminate and B for bonding), (c) TWO (for two laminates), and (d) 2T (2 for two-laminate and T for taping)

- B. 2B – As shown in Figure 4.4(b), both u-fringes and v-fringes revealed good bonding in the 2B case since the discontinuity of u-fringes across the bonding interface was insignificant. The difference of v-fringes between the 2B case and the ONE case was believed to result from the difference of initial fringes at no-loading condition.
- C. TWO – The u-fringes and v-fringes were shown in Figure 4.4(c). Both fringes in each laminate of the beam seemed to be very independent. Each pattern seemed to resemble the corresponding pattern of the ONE case up to some extent.
- D. 2T – As shown in Figure 4.4(d), the fringe patterns seemed to be similar to those of the TWO case. It implied that the bonding due to the double-coated tapes used in the study was very poor.
- E. 2R2 – Although the v-fringes were kinky across the joining interface, implying imperfection of joining, the u-fringes (shown in Figure 4.5(a)) were like those of the 2B case. The results seemed to indicate that two rivets per 50 mm were sufficient for joining the composite laminates, at least for the 45 N used in the investigation.
- F. 2R3 – Shown in Figure 4.5(b), the u-fringes were like those of the 2R2 case except some isolated irregularities. Since the v-fringes of the 2R3 case were less kinky across the joining interface than those of the 2R2 case, the former seemed to be a better joint than the latter.

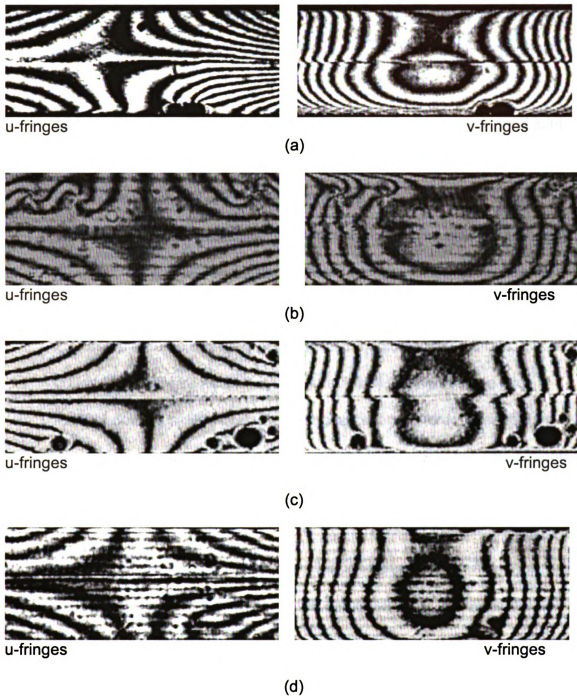
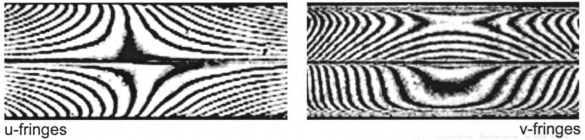


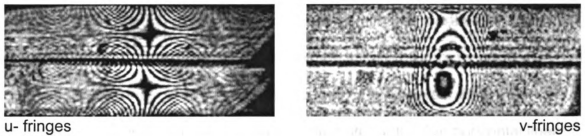
Figure 4.5 - Moiré fringe pattern for: (a) 2R2 (the first 2 for two-laminate, R for riveting and the second 2 for two rivets per 50 mm), (b) 2R3 (R for riveting and 3 for three rivets per 50 mm), (c) 2R4 (R for riveting and 4 for four rivets per 50 mm), and (d) 2BR3 (B for bonding, R for riveting and 3 for three rivets per 50 mm)

- G. 2R4 – Shown in Figure 4.5(c), the moire fringe patterns of the 2R4 case were similar to those of the 2R3 case, implying a similar joining condition in the two cases.
- H. 2BR3 – Based on Figure 4.5(d), 2BR3 apparently was a very good joint.
- I. 2S3 – Similar to other cases, 2S3 was loaded by four-point bending. Before the breakage of the stitching lines, e.g. at 45 N, the u-fringes, shown in Figure 4.6(a), resembled those of the ONE case. The v-fringes, however, were of two separated patterns though not as independent as those of the TWO case. As compared with 2R2, the joining condition of 2S3 seemed to be relatively poor. Once the stitching lines broke, e.g. at 200 N, the u-fringes as shown in Figure 4.6(b) clearly became two independent sets. However, the v-fringes became more dependent on each other possibly due to the high contact-friction between the laminates at the high loading level.
- J. 2S5 – The u-fringes shown in Figure 4.6(c) revealed that 2S5 was a good joint. The v-fringes, however, showed a great deal of discontinuity across the joining interface. According to the fringe patterns, the two laminates in the 2S5 case seemed to have a closer interaction than those in the 2S3 case, indicating that 2S5 was a better joint than 2S3.
- K. 2BS3 –As shown in Figure 4.6(d), the fringe patterns of 2BS3 were very similar to those of 2B. Apparently, epoxy bonding outperformed the stitching joining and played the dominant role in the 2BS3 case.

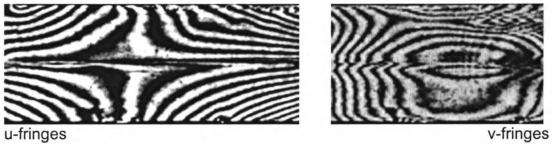




(a)



(b)



(c)



(d)

Figure 4.6.- Moire fringe patterns of various joining subjected to four point bending: (a) 2S3 (90N) (S for stitching and 3 for three stitches per 50 mm), (b) 2S3 (200 N) , (c) 2S5 (S for stitching and 5 for 5-by-2 stitching pattern), and (d) 2BS3 (B for bonding, S for stitching and 3 for three stitches per 50 mm)

## **Maximum joining force**

Before the joining forces in various assembled composite beams are calculated, the ONE case should be carefully examined because it could be used as basis for comparison of the joining forces. To begin with, moire fringe orders were assigned to the u-fringes, i.e  $N_x$ , as shown in Figure 4.7(a). The fringes in Figure 4.7(a) were identical to those in Figure 4.7(a). Both were obtained from  $P = 22.5$  N. Five locations through the laminate thickness were then selected and horizontal lines at the five locations were added to the Figure 4.7(a). Relations between the u-fringe order  $N_x$  and the  $x$ -coordinate for the five horizontal lines were established and given in Figure 4.7(b). The normal strain, however, could be obtained from combining the displacement-fringe relation ( $u = \frac{N_x}{f}$ ) and the linear strain-displacement relation ( $\varepsilon_x = \frac{\partial u}{\partial x}$ ), i.e.

$$\varepsilon_x = \frac{1}{f} \frac{\partial N_x}{\partial x} \quad (4.16)$$

In the study, the system frequency  $f$  was 2400 lines/mm. It was twice the frequency of moire grating.

The normal strain given in Equation (4.16) was, in fact, the slope of the  $N_x$ - $x$  relation. From Figure 4.7(b), the strains at the five locations along the  $y$ -axis could be identified. They were shown in Figure 4.7(c) with solid circles. A solid line based on least-squares analysis was also presented. Apparently, the solid circles matched very well with the least-squares line, indicating that the strain

distribution was linear through the laminate thickness. This result was consistent with the assumptions of the Classical Beam Theory imposed in the analytical modeling and the small loading utilized in the experimental investigations.

As mentioned earlier, the moire fringes were not of null field at no-loading condition. By subtracting the residual strains at  $P = 0$  from those at  $P = 22.5$  N (Figure 4.7(c)), the real strains due to external loading could be obtained. Based on the real strains and  $P = 22.5$  N, the Young's modulus of the composite laminate was found to be 22.27 GPa. This value was used in subsequent calculations.

In addition to the perfect-joining case ONE, the experimental result of an imperfect-joining case 2B was also obtained. For comparison, they were both depicted on Figure 4.6. Since the thickness of the ONE case was 3.2 mm and that of 2B was 6.6 mm, a magnification factor of 4 according to the flexure formula was imposed on the ONE case.

As shown in Figure 4.8, the normal strains in the perfect-joining case could be represented by a single straight line through the laminate thickness whereas those of the imperfect-joining case two straight lines, one on each layer. Apparently, the strain distribution of an assembled two-layer composite beam was strongly affected by the joining condition. Figures 4.9(a), 4.9(b), and 4.9(c) showed schematic diagrams of the normal strains in three assembled beams with perfect joining, imperfect joining and no joining, respectively.

The normal strains represented by a solid line in Figure 4.7(a) were continuous across the joining interface in the perfect-joining case. They could be obtained from the flexure formula by assuming that the perfectly joined beam was a single beam with double thickness.

The normal strains in the imperfect-joining case then should be between the two extreme cases, as concluded from the 2B case shown in Figure 4.8. The schematic diagram for the imperfect-joining case was shown in Figure 4.9(b).

The normal strains in the no-joining case as shown in Figure 4.9(c), however, were of two identical but independent dashed lines, indicating that each layer behaved independently. Accordingly, the joining force  $F_j$  presented in the analytical modeling was created for joining the composite layers together. The higher the joining force, the less the mismatch of the normal strains, and the normal strains, across the joining interface.

In addition to identifying the Young's modulus of the composite laminate, the u-fringes from ONE case could also be used to identify the theoretical value of maximum joining force in perfectly joined composite beams. The ONE case, on one hand, can be considered as being made up of two composite layers (each has a thickness equal to one half of the total thickness of the ONE beam) with perfect joining. Recalling Equation (4.7), the normal stress in layer (1) is

$$\sigma_x^{(1)} = -\frac{F_1}{A_1} + \frac{F_1 h_1}{2I_1} y_1 - \frac{M}{2I_1} y_1 \quad (4.7)$$

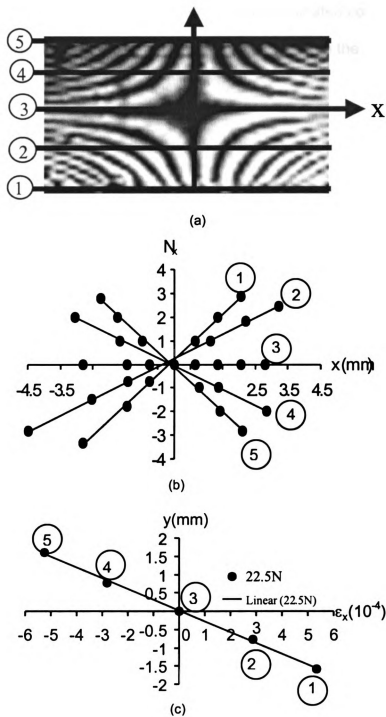


Figure 4.7 - Normal strain calculations, (a) moiré fringe pattern for ONE case in five designated locations, (b) relation between u-fringes and  $N_x$  in five locations, and (c) strains in the five locations along y-axis

where  $I_1 = \frac{bh_1^3}{12}$  and  $h_1$  is one half of the total thickness  $h$  of the ONE beam. On the other hand, the ONE case is actually a single laminated composite beam. And the normal stress in the beam can be calculated from the flexure formula, i.e.

$$\sigma_x^{(1)} = -\frac{MY}{I} \quad (4.17)$$

where  $Y = y_1 + h/4$  and  $I = \frac{bh^3}{12}$ .

By equating Equations (4.7) and (4.17), it yields

$$F = \frac{3M}{2h} \quad (4.18)$$

Apparently, the joining force in the two composite layers perfectly joined together is dependent on the total bending moment  $M$  due to the transverse loading and the total thickness of the assembly  $h$ . In other words, there is a theoretical joining force for perfectly joined composite beams. For example, by substituting  $M = 562.5$  Nmm (based on  $P = 22.5$  N and 25 mm between the outer roller and the inner roller as shown in Figure 4.2(a)) and  $h = 6.4$  mm (for a two-laminate beam) into Equation (4.18), a joining force of 139 N is obtained.

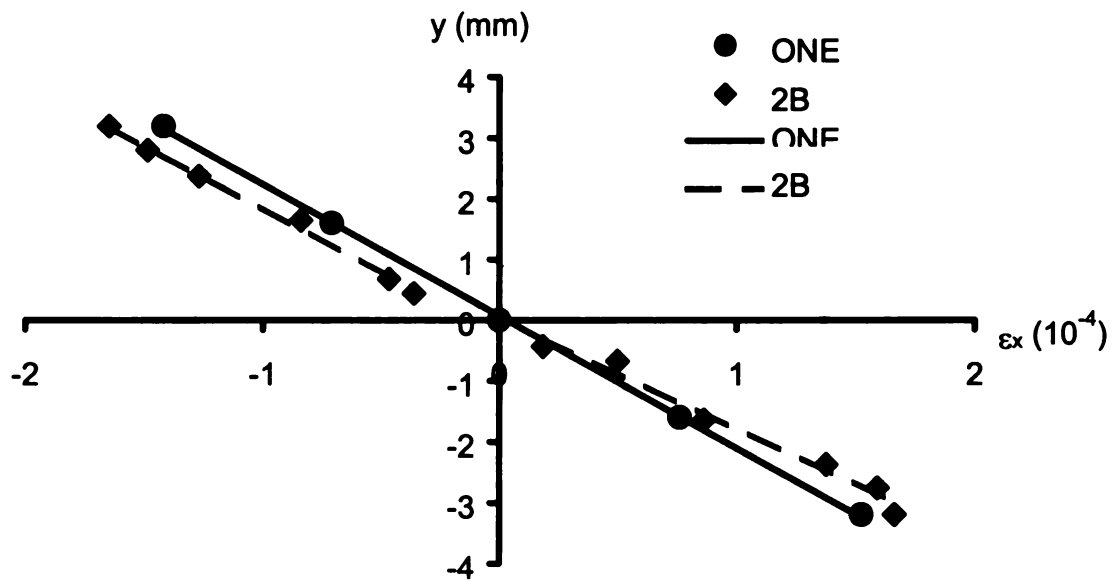


Figure 4.8 - Comparison of normal strain for perfect bonding ONE and imperfect bonding 2B

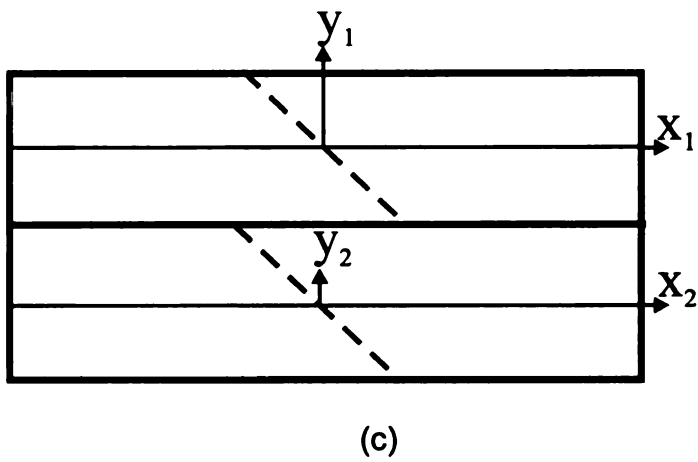
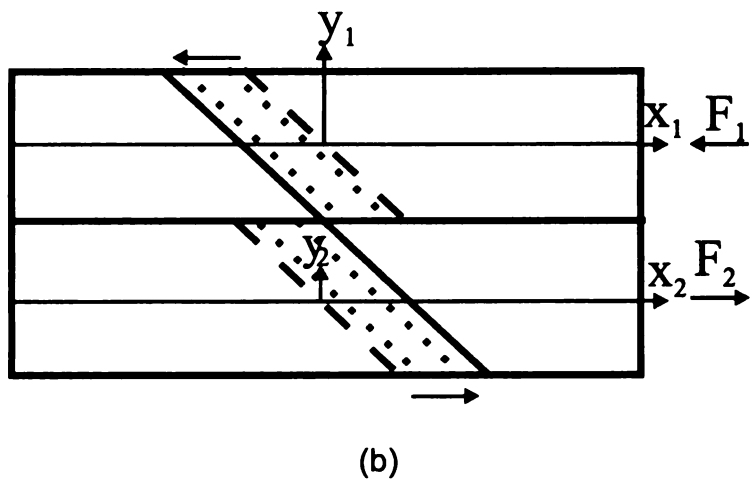
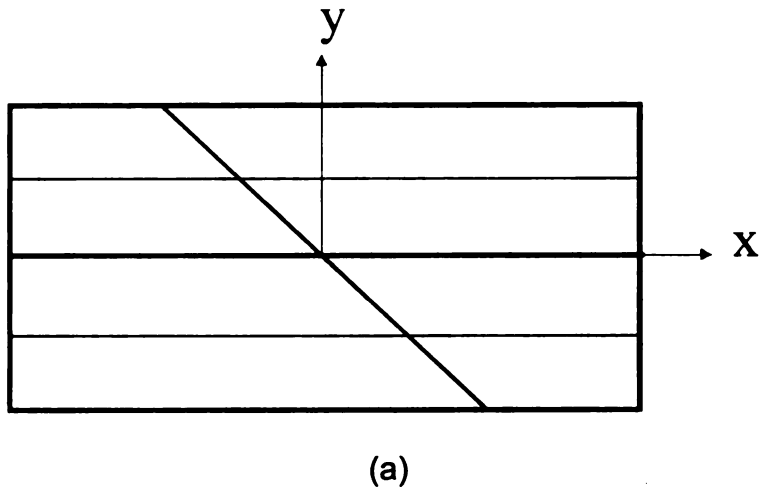


Figure 4.9 - Schematic diagram for: (a) perfect bonding, (b) imperfect bonding, and (c) no bonding



## Singular points

Equation (4.7) is valid for all joining conditions, good joining as well as poor joining. Both equations are organized by two parts: one associated with the joining force  $F_i$  and the other associated with the total bending moment  $M$ . Since only the joining force is dependent on the joining condition, only the part associated with the joining force is affected by the joining condition.  $M$  is actually calculated from the flexure formula.

By setting the part associated with the joining force equal to zero, i.e.

$$-\frac{F_1}{A_1} + \frac{F_1 h_1}{2I_1} y_1 = 0, \quad (4.19)$$

it can be found that the normal stress is only dependent on the total bending moment  $M$  when

$$y_1 = \frac{h_1}{6}. \quad (4.20)$$

Substituting Equation (4.20) back into Equation (4.7), yields

$$\sigma_x^{(1)} = -\frac{M}{bh_1^2} \quad (21)$$

Equation (4.21) gives an invariant normal stress at  $y_1 = h_1/6$ . Similarly, it can also be found that  $\sigma_x^{(2)} = \frac{M}{bh_2^2}$  at  $y_2 = -h_2/6$ . These two locations, i.e.  $y_1 = h_1/6$

and  $y_2 = -h_2/6$ , are called *singular points* since the normal stresses of assembled two-laminate beams at these two points are independent of joining condition.

As a resultant component, the joining force  $F_j$  should be constant in each joining case. However, by closely examining Equation (4.7), it was found that  $F_j$  fluctuated around the singular points due to numerical sensitivity. Figure 4.10 showed the comparison between the analytical predictions based on Equation (4.7) and the experimental results for the ONE case. The joining force became singular at the singular points. It then was suggested that the experimental measurements should avoid the neighborhood of the singular points. Since the density of moire fringes was usually quite low close to the joining interface, e.g. Figure 4.4(b) for the 2B case, the beam surfaces were thus concluded as better locations for joining analysis. In addition, it should be noted that good agreements between the analytical predictions and the experimental results, as shown in Figure 4.8, for many locations through the beam thickness were obtained.

The analytical modeling was based on two-dimensional approach and the experimental investigation was actually of three-dimensional analysis. As a result, the good agreements between them suggested that the free-edge effect, which was usually considered as an important phenomenon in laminated composite materials [4.7], should not be of a major concern in the study.

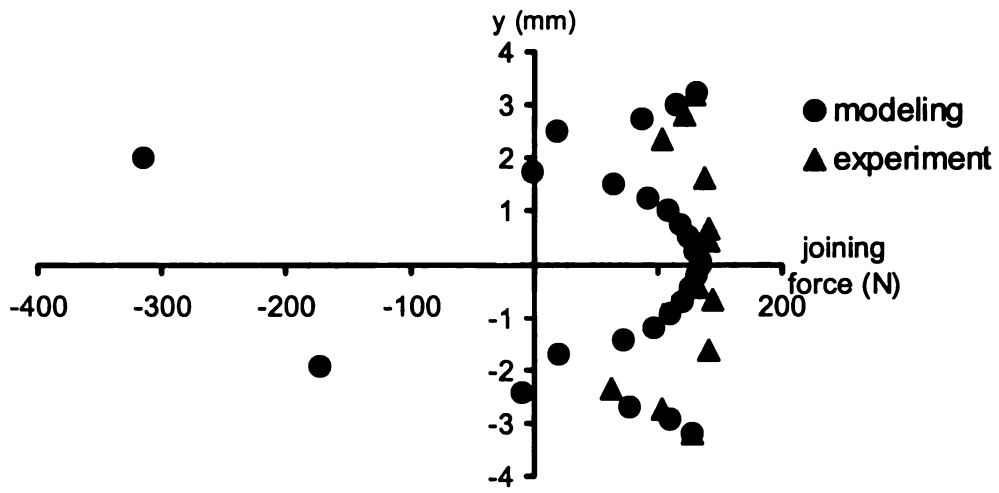


Figure 4.10 - Comparison between analytical predictions and experimental results

## Joining forces

The top and bottom surfaces were better locations than the mid-plane for joining analysis because of their high density of moire fringes. They were also better than points close to the singular points because of stable stress distribution. To identify the joining forces of various assembled beams, the normal strains at the surfaces were obtained by subtracting the strains due to  $P = 45$  N from those due to  $P = 67.5$  N. This procedure was based on the fact that the moire fringe patterns in the assembled beams were not of null field at no-loading condition.

For the ONE case, the joining force based on Equation (4.18) was 132 N while those obtained from experiments based on both surfaces were 139 N. They agreed quite well. By using experimental results and Equation (4.7), the joining forces based on both surfaces for various types of joining were also obtained and listed in Table (4.1). Results from the top surfaces seemed to agree with those from the bottom surfaces. All the joining forces were also normalized by that of the perfect joining case, i.e. ONE, for comparison. A similar procedure was also performed for the interphase model based on Equation (4.14). The results from the interphase model were, in fact, the averages of the corresponding values obtained from the top and bottom surfaces based on the interface model.

| Interface Model |                   |      |                   |     | Interphase Model                   |     |
|-----------------|-------------------|------|-------------------|-----|------------------------------------|-----|
|                 | top surface       |      | bottom surface    |     | (based on top and bottom surfaces) |     |
|                 | joining force (N) | %    | joining force (N) | %   | joining force (N)                  | %   |
| ONE             | 139               | 100  | 139               | 100 | 139                                | 100 |
| 2B              | 123               | 88   | 125               | 89  | 124                                | 89  |
| TWO             | -139              | -100 | -137              | -98 | -138                               | -99 |
| 2T              | -31               | -22  | -7                | -5  | -19                                | -13 |
| 2R2             | 124               | 89   | 128               | 92  | 126                                | 90  |
| 2R3             | 138               | 99   | 139               | 100 | 139                                | 100 |
| 2R4             | 142               | 102  | 144               | 103 | 143                                | 102 |
| 2BR3            | 132               | 95   | 141               | 101 | 137                                | 98  |
| 2S3             | 97                | 70   | 77                | 55  | 87                                 | 62  |
| 2S5             | 111               | 80   | 110               | 79  | 111                                | 79  |
| 2BS3            | 124               | 89   | 122               | 87  | 123                                | 88  |

Table 4. 1- Comparisons of joining forces

According to Table (4.1), the joining force of the 2B case was not as high as the perfect bonding case, ONE, indicating that the epoxy used in the study gave an imperfect-joining result. The joining forces of 2R2 and 2R3 were very close to that of ONE while the joining force of 2R4 was actually higher than that of ONE. It was believed that the high joining forces were attributed to the excellent joining conditions based on riveting and the rigidity of the rivets themselves. Comparing the 2R2, 2R3 and 2R4 cases reveals that the joining force increased as the density of rivets increased. A similar result could be found from comparing the 2S3 and 2S5 cases.

The comparison of the joining forces of 2BR3, 2R3 and 2B revealed that the mechanical riveting was more efficient than the epoxy bonding. The mechanical riveting alone was sufficient for joining the composite beams. The epoxy bonding, in fact, played a redundant role in the 2BR3 case. The comparison of the 2BS3, 2S3 and 2B cases indicated that epoxy bonding was more efficient than stitching joining. And gain, the less efficient technique, i.e. stitching joining, played a redundant role in the case based on combined techniques, i.e. 2BS3. The negative joining forces of the TWO and 2T cases were not clear although they were both of poor joining cases.

## **Conclusions**

1. Although it is a surface technique, moire interferometry is able to give a whole-field analysis, e.g. through-the-thickness measurement. Due to

transverse loading, the free-edge effect can be neglected in the investigation of normal strains. In addition, the surface points are found to be better than other locations through the thickness of a composite beam for normal strain analysis because the density of the moire fringes are higher and the stresses are relatively uniform close to the surfaces.

2. Though based on the Classical Beam Theory, both the interface model and the interphase model are capable of presenting joining forces of assembled composite beams with the use of moire interferometry. Good agreements between analytical predictions and experimental investigations seem to indicate that it is feasible to use the technique combining analytical models and moire interferometry for identifying joining forces.
3. Among the joining techniques investigated in the study, mechanical riveting seems to be an efficient joining technique because it is easy to employ and can give high joining force.

## **Acknowledgments**

The author wishes to express his sincere thanks to Professor Dan Post of Virginia Polytechnic Institute and State University for help in constructing the moire interferometer used in this study and many valuable discussions on the fundamentals of moire interferometry. Thanks are also extended to Professor Peter Ifju of University of Florida for providing the original moire gratings from

which many gratings used in this study were derived. The financial support from the Michigan Research Excellence Fund is also greatly acknowledged.



## References

- 4.1 Y. D. S. Rajapakse, ed., *Mechanics of Thick Composites*, AMD-Vol. 162, The American Society of Mechanical Engineers, 1993.
- 4.2 Liu, D. and B.B. Raju, "Effects of Joining Techniques on Impact Perforation Resistance of Assembled Composite Plates," to appear in *Experimental Mechanics*.
- 4.3 Liu, Dahsin, "Delamination Resistance in Stitched and Unstitched Composite Plates Subjected to Impact Loading," *J. Reinforced Plastics and Composites*, 9 (1), 59-69, 1990.
- 4.4 Lee, Chienhom and Liu, Dahsin, "Tensile Strength of Stitching Joint in Woven Glass Fabrics," *J. Engineering Materials and Technology*, 112 (2), 125-130, 1990.
- 4.5 Liu, Dahsin and Shakour, Elias, "Combining Photoelasticity and Moire Interferometry," submitted to *Experimental Mechanics*.
- 4.6 Post, D., Han, B. and Ifju, P., *High Sensitivity Moire*, Springer-Verlag, 1991.
- 4.7 Pipes, R.B. and Pagano, N.J., "Interlaminar Stresses in Composite Laminates under Uniform Axial Extension," *J. Composite Materials*, 4, 538-548.

## Chapter 5

### CONCLUSIONS AND RECOMENDATIONS

This thesis work was composed of four chapters. Chapter 1 introduced the moire technique and gave a literature review on the moire grating and its advancement towards the sensitivity enhancement of the measurement technique. Then, a various applications were introduced in experimental mechanics that utilized the moire interferometry technique.

Chapter 2 described the modification of the grating layers from a conventional two-layer grating, to a one-layer grating, and finally a zero-layer grating (self grating). The optical moire interferometer setup was also modified to include either transparent photoelasticity setup or reflective photoelasticity setup, namely combining moire interferometry with photoelasticity. A photoelastic sensitive epoxy named PL8 was molded as a zero-layered grating and served as a coating layer to measure the stress concentrations of a drilled hole in a glass/epoxy specimen.

Chapter 3 presented a comprehensive study on the relationship between the mismatches of material properties and the free edge effect. In the investigations, the one-layer grating was bonded on the surface of a graphite/epoxy, a composite laminates with a stacking sequence of [0/90/0/90/0/90/0] and on the surface of glass/epoxy composite laminates with

stacking sequences of  $[0_7/90_7/0_7]$ ,  $[0_3/90_3/0_3/90_3/0_3/90_3/0_3]$ , and  $[0/90/0,\dots]_{21}$ . The investigations identified: the depth of the boundary layer; it also verified the effect of material type, between graphite/epoxy and glass/epoxy, and the effect of lamination type, among the 3-lamina, 7-lamina, and 21-lamina laminates.

Chapter 4 described using the one-layer grating to conduct a study on the joining forces of assembled thin laminated composites. The one-layer grating was bonded onto the edge of the laminated beams. The beams were assembled by using various joining techniques, such as mechanical riveting, adhesive bonding, stitching joining and their combination. Based on the Classical Beam Theory, the interface model and the interphase model were compared with those of experimental results.

## **Major conclusions**

### ***Chapter two***

1. A simplified two-layer grating technique was developed. Two-layer grating could be further simplified to one-layer grating by simply omitting the enhancing layer, i.e. aluminum layer. The one-layer grating technique was found to be feasible for moire measurements.
2. A zero-layer grating technique was developed. The advantage of the one-layer technique is that it does not have thickness; neither is there a mismatch of material properties between the specimen and the zero-layer.

3. A technique combining moire and photoelasticity was capable of presenting two independent sets of experiment and result. This technique provides a self-verification capability by comparing both sets of results.

### ***Chapter three***

1. Experimental results based on moire interferometry have revealed that the shear strain on the free-edge increase significantly as the width of a composite laminate decreases.
2. Because of the free edge-effect, shear strain based on moire interferometry should not be used beyond the surface at all.
3. The depth of the boundary layer was found based on moire interferometry is greater than the thickness of composite laminates.
4. The free edge-effect is associated with mismatch of material properties. Since graphite/epoxy has higher anisotropy than glass/epoxy, a composite laminate made of graphite/epoxy experiences stronger free-edge effect than the glass/epoxy counterpart.
5. Normal strains on free edges are not influenced by the free edge effect. Accordingly, the normal strains based on moire interferometry could be used to represent the normal strains beyond the surface for plane-strain and plane stress problems.

## **Chapter four**

1. Moire interferometry is able to give a whole-field analysis, e.g. the edges through the laminate thickness, although it is a surface measurement technique. The free-edge effect can be neglected in the investigation of the normal loading.
2. Both the interface model and the interphase model present joining forces of assembled composite beams based on the Classical Beam Theory with the use of moire interferometry. It is feasible to use the technique of combining analytical models and moire interferometry for identifying joining forces.
3. Mechanical riveting seems to be an efficient joining technique because it is easy to employ and can give a high joining force.

## **Recommendations for future work**

1. Investigators should explore modifying the diffraction grating. A technique must be able to attach the diffraction grating onto the surface of the specimen in a technique similar to the strain-gage installment. Using this modification will allow the moire nterferometry to be less complicated and more friendly especially when conducting testing in a field position.

2. Investigators should explore building a micro-scale moire interferometer that can be positioned in front of an optical microscope to measure within the micro mechanics field, such as the interface interphase between fibers and matrices.

## **APPENDICES**

## APPENDIX A

### PROCEDURES FOR ALUMINUM EVAPORATION

The machine that was used for aluminum evaporation is Bendex- Balzer Vacuum Inc. (Rochester, NY). The operation was as follows:

1. Position the Tungsten wire in a 17 inches height above the grating.
2. Lay down the master grating.
3. Close the bell jar.
4. Pump down the diffusion pump.
  - a. gauge to V2.
  - b. lever to 1.
  - c. pump to 0.05 torr.
5. Pump down the bell jar.
  - a. Lever to 3.
  - b. gauge to H..
  - c. pump to  $5 \times 10^{-7}$  torr.
6. Turn the Quartz Crystal Thickness monitor on.

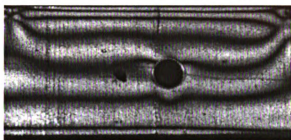


7. Turn the current switch on.
  
8. Monitor the Quartz Crystal till it reaches the desire thickness ( for aluminum; 1.3 hz→1 Å on the quartz Crystal monitor.)

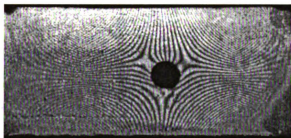
## APPENDIX B

### MOIRE FRINGE PATTERNS USED FOR SUBTRACTIONS

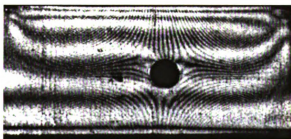
#### Combining moire interferometry and photoelasticity



(a)



(b)



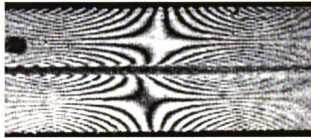
(c)

Figure A.1- Fringe patterns of a notched glass/epoxy beam with PL8 moire-photoelasticity coating (344.72 N) (a) reflection isochromatic fringes, (b) U-displacement fringes, and (c) simultaneous recording of photoelasticity and moire fringes.

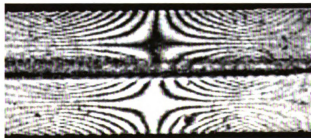
## Joining forces in assembled composites



(a)



(b)

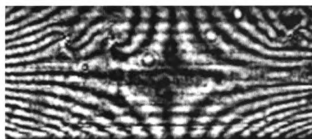


(c)



(d)

Figure A.2 - Moire Fringe pattern for 67.5 N, (a) 2B, (b) TWO, (c) 2T, and (d) 2R2



(a)



(b)

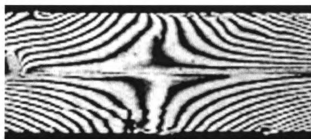


(c)



(d)

Figure A.3 - Moire fringe patterns (67.5 N) (a) 2R3, (b) 2R4, (c) 2BR3, and (d) 2S3



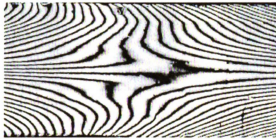
(a)



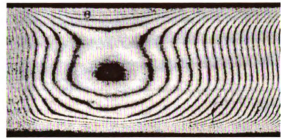
(b)

Figure A. 4 - Moire fringe patterns (67.5 N), (a) 2S5, and (b) 2BS3

## Mismatch of materials and the free edge effect

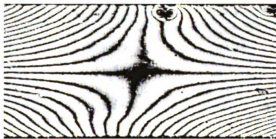


u-fringes

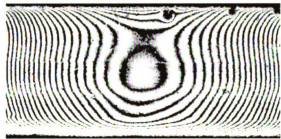


v-fringes

(a) 25.4 mm, 889.6 N

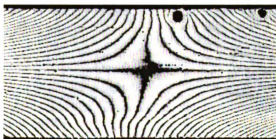


u-fringes

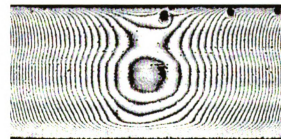


v-fringes

(b) 12.7 mm, 444.8 N



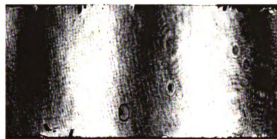
u-fringes



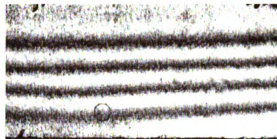
v-fringes

(c) 6.35 mm, 222.4 N

Figure A.5 - Moiré fringe patterns for graphite/epoxy laminates with three different widths



u-fringes

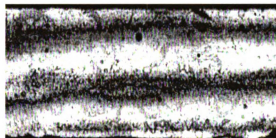


v-fringes

(a) 3-lamina mm, zero load



u-fringes

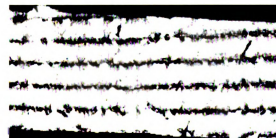


v-fringes

(b) 7-lamina, zero load



u-fringes



v-fringes

(c) 21-lamina, zero load

Figure A.6 - Moire fringes of glass/epoxy laminates at a zero load

MICHIGAN STATE UNIVERSITY LIBRARIES



3 1293 02088 0872